Lattice modelling of complete acoustic emission waveforms in the concrete fracture process

Zhou, Yubao; Aydin, Beyazit Bestami; Zhang, Fengqiao; Hendriks, Max A.N.; Yang, Yuguang

DOI
10.1016/j.engfracmech.2025.111040

Publication date
2025

Document Version
Final published version

Published in
Engineering Fracture Mechanics

Engineering Fracture Mechanics 320 (2025) 111040

Contents lists available at ScienceDirect

Engineering Fracture Mechanics

journal homepage: www.elsevier.com/locate/engfracmech

Lattice modelling of complete acoustic emission waveforms in the concrete fracture process

Yubao Zhou [a,*], Beyazit Bestami Aydin [a,b], Fengqiao Zhang [a], Max A.N. Hendriks [a,c], Yuguang Yang [a]

[a] *Faculty of Civil Engineering and Geosciences, Delft University of Technology, 2628CN Delft, the Netherlands*
[b] *Department of Civil Engineering, Middle East Technical University (METU), 06800 Ankara, Turkey*
[c] *Department of Structural Engineering, Norwegian University of Science and Technology, 7491 Trondheim, Norway*

ARTICLE INFO

Keywords:
Acoustic emission (AE)
Concrete fracture
Dynamic lattice model
Full-waveform analysis
Structural health monitoring (SHM)

ABSTRACT

The next generation of acoustic emission (AE) applications in concrete structural health monitoring (SHM) relies upon a reliable and quantitative relationship between AE measurements and corresponding AE sources. To achieve this, it is a prerequisite to accurately model the whole AE process that is a multiscale coupling process between local material fracturing and induced elastic wave propagation at structural level. Such a complex process, however, cannot be well addressed in currently available modelling methods. To fill this research gap, this study proposes a lattice modelling approach that achieves for the first time the explicit simulation of complete waveforms of transient AE signals induced by concrete fracture. The proposed approach incorporates an explicit time integration technique with a novel proportional-integral-derivative (PID) control algorithm for reducing spurious oscillations and a Rayleigh damping-based calculation and calibration method for the attenuation of AE waves. In this paper, the proposed lattice modelling approach is implemented to simulate the concrete Mode-I fracturing process in a three-point bending test. Besides the mechanical behaviors and AE hit number, a comparison was conducted between numerically and experimentally obtained AE waveforms. The AE waveforms and their attenuation characteristics simulated by the proposed lattice modelling method turn out to be comparable to experimental results. The proposed approach is of significance for a deep understanding of AE-related fracture mechanisms and a more reliable application of AE technique.

1. Introduction

Acoustic emission (AE) refers to the transient elastic waves induced by rapid energy release during some transient irreversible stress redistribution processes at local material regions (AE sources) [1]. The induced elastic waves travelling within structures can be captured and transformed into electrical signals (AE signals) by AE sensors mounted on structure surfaces. The obtained signals are further processed with various techniques with the aim of characterizing internal signal sources, such as the type [2,3] and location of AE sources [4,5]. Reliable applications of AE technique rely upon a quantitative relationship between AE measurements and corresponding signal sources.

* Corresponding author.
E-mail addresses: y.zhou-16@tudelft.nl (Y. Zhou), b.b.aydin@tudelft.nl (B.B. Aydin), f.zhang-5@tudelft.nl (F. Zhang), M.A.N.Hendriks@tudelft.nl (M.A.N. Hendriks), Yuguang.Yang@tudelft.nl (Y. Yang).

https://doi.org/10.1016/j.engfracmech.2025.111040
Received 7 October 2024; Received in revised form 21 January 2025; Accepted 12 March 2025
Available online 15 March 2025
0013-7944/

Nomenclature

AE	acoustic emission
CMOD	crack mouth opening displacement
DEM	discrete element method
FEM	finite element method
HDT	hit definition time
HLT	hit lockout time
LVDT	linear variable differential transducer
MMT	moment tensor
PID	proportional-integral-derivative control
SHM	structural health monitoring
PDT	peak definition time
PLB	pencil lead break
A	wave amplitude
A^*	effective cross-section area
$\overline{A}$	average wave amplitude
A_{sensor}	wave amplitude with "sensor effect"
$A^{(normalized)}$	normalized wave amplitude
a_1	first tensile softening parameter
a_2	second tensile softening parameter
a_3	third tensile softening parameter
b_1	first stress reduction parameter
b_2	second stress reduction parameter
$\boldsymbol{C}$	damping matrix
D	sensor diameter
Δd_{max}	maximum sensor spacing distance
E	Young's modulus
$e(t)$	PID tracking error
$\boldsymbol{F}$	internal nodal force vector
F	nodal force
F_e	element force
f_c	compressive strength
$f_{c,cube}$	cube compressive strength
f_{Ny}	Nyquist frequency
f_s	sampling frequency
f_t	tensile strength
G_f	fracture energy
h	lattice grid size
$\boldsymbol{K}$	stiffness matrix
K_p	proportional PID parameter
K_i	integral PID parameter
K_d	derivative PID parameter
l	lattice element size
$\boldsymbol{M}$	mass matrix
m	mass of a wave particle
n	number of nodes
$\boldsymbol{P}(t)$	external force vectors
$\dot{P}(t)$	external loading rate
$S(\omega)$	sensor sensitivity function
S	sensor area
s_i	representing area of node i
t	Time
t_{max}	total processing time
Δt	time step
Δt_{max}	maximum trvavel time difference
$\boldsymbol{u}$	displacement vector
u	nodal displacement
$\dot{\boldsymbol{u}}$	velocity vector

$\dot{u}$	nodal velocity
$\ddot{\boldsymbol{u}}$	acceleration vector
$\ddot{u}$	nodal acceleration
V	wave velocity
V_p	pressure wave velocity
$\Delta v(t)$	nodal velocity difference
$\Delta v_0(t)$	targeted nodal velocity difference
w_i	area weight of node i
α	mass-proportional damping coefficient
β	stiffness-proportional damping coefficient
λ	wavelength
η	material damping factor
ε	element strain
ε_{cr}	cracking strain
ω	wave angular frequency

A reliable signal-to-source relationship is, however, not trivial. Characterizing local signal sources through AE measurements is a typical inverse problem. Although carrying the information of sources, the received AE signals are also influenced by many other factors, such as wave propagation and AE sensor response. Although many AE source characterization approaches have been proposes in literature [6–9], none of them can provide a reliable relationship between signal sources and received AE signals, as the influence from wave propagation and sensor response cannot be removed. Different or even conflicted conclusions can be drawn from the phenomenological methods when applied to different experimental cases [10].

Alternatively, we propose to explicitly model AE signals using a forward approach. Compared to the phenomenological models, forward-modelling methods are more reliable to understand and further establish relationships between the signal sources and the received signals, in which the signal source, wave propagation and sensor response can be separately considered. Amongst various AE sources, concrete fracturing is one of the major origin of AE signals and is often used to indicate the health conditions of concrete structures [11]. Therefore, this paper will focus on the modelling of the AE signals generated by the fracturing processes of concrete only. Furthermore, tensile cracking at fracturing process zone (crack tip) and friction along existing cracking surfaces are two main AE source types involved in concrete fracturing processes [4]. At the first step, this paper deals with the AE source type of concrete tensile cracking, as it is the most forward AE sources induced by concrete fracture while its physical basis to generate AE signals remains unclear.

After a comprehensive literature review on available AE modelling methods in Section 2, we demonstrate that accurate modelling of the complete AE process during concrete fracturing is challenging. Among others, the lattice type models are considered promising for AE simulation as they are mature methods for concrete fracturing simulation. The lattice modelling has been adopted to simulate the fracture processes and induced AE phenomena in various quasi-brittle materials [12–14]. Nevertheless, an accurate simulation of elastic wave propagation by lattice modelling has not yet been achieved, although the material fracturing processes have been well modelled in available work in a dedicated way. Therefore, explicit simulation of the complete transient waveforms of fracture-induced AE signals by lattice modelling is still a pending challenge. Here the major challenge lies in the lack of a consistent and reliable method to simulate both the fracturing process of concrete and elastic wave propagation within a same lattice modelling approach. In previous research by the same authors [15,16], several techniques have been established within the lattice model framework concerning simulating the propagation of AE included elastic waves in concrete.

In this paper, through an example of a three-point bending test of an unreinforced concrete beam, we will demonstrate a consistent lattice modelling approach that can, for the first time in literature, simulate: the fracturing processes of concrete, the propagation of AE included elastic waves, and eventually the collection of wave signals through AE sensors. Without further calibration, the simulated AE waveforms resemble the measured ones in the experiment.

2. Review and discussion on AE modelling methods in literature

A literature review on available AE modelling methods is given in this section. Available AE modelling methods can be mainly classified into four categories, including analytical models, finite element methods (FEM), particle-based discrete element methods (DEM) and lattice models. To model the complete AE process, it requires a model to consider both local AE sources and global wave propagation. In the following, we discuss the pros and cons of each available modelling method in these two aspects.

2.1. Analytical model

Among available analytical treatments, the moment tensor (MMT) theory [17–19] is the most used analytical method in AE field. Several attempts have been made to quantify concrete fracturing behavior using MMT, such as fractured volume estimation [20,21] and AE source type classification [22,23] through MMT inversion. However, the MMT involves several strong assumptions:

- AE sources induced by material fracture in the MMT are assumed as a displacement discontinuity, which is further represented by an equivalent third-order force tensor, called moment tensor [19,24]. Moment tensor representation can only describe the magnitude and motion direction of a crack, while the dynamic history of cracking is based on an assumed source-time function [25,26].
- Wave propagation in the MMT is modelled by solving Green's function [19,24]. The Green's function used in MMT is derived under the assumption of a semi-infinite half-space [27,28] and thus cannot consider the complicated wave propagation in real concrete structures.

2.2. FEM

The finite element method (FEM) is one of the most used numerical methods for AE simulations. Although it is suitable for simulating elastic wave propagation, the FEM cannot well describe local fracture-induced AE sources.

- Fracture-induced AE sources in typical FEM-based AE simulations are usually indirectly introduced as an external input by a displacement–time function [29,30], a monopole/concentrated force [31,32] or a pair of dipole/couple forces [33,34]. Similarly to the analytical MMT, an assumed source-time function is used to describe the dynamic history of an AE source [35,36]. The FEM and other continuum theory-based methods established on the basis of continuity hypothesis and local contact principle cannot explicitly simulate the local displacement discontinuity (namely fracture-induced AE sources) [37,38].
- Wave propagation in the FEM is simulated by solving motion equations [33] or wave equations [39]. These governing equations established in terms of partial differential equations are field equations that rigorously describe the wave field. FEMs have been extensively implemented in simulating the propagation of AE waves induced by assumed source functions in different materials [32,33,35,40,41].

2.3. Particle-based DEM

In particle-based discrete element methods (DEM), materials are conceptualized as an amalgamation of rigid or deformable particles. The interaction between particles is described by micromechanical bonds at their contacts. Particle-based DEM is suitable for solving discontinuous problems and thus for AE source modelling, while it faces difficulty in accurately simulating the wave propagation.

- Fracture-induced AE sources in particle-based DEM are analogous by bond breakages (failure of contact forces) [42–44]. The use of bond forces for the description of internal forces avoids the stress singularity at crack tip; therefore, particle-based DEM can realistically simulate the microscopic fracturing phenomenon [43,45]. The particle-based DEM models have been extensively employed to simulate the fracture-induced AE events in different brittle and quasi-brittle materials [46–50].
- Similarly to the FEM, wave propagation in particle-based DEM is also simulated by solving motion equations [51,52]. However, the governing equations (motion equations) in particle-based DEM are established based on local contact forces between particles. Such discrete equations of local contact force equilibrium cannot rigorously describe the global wave field [53,54]. Due to such a limitation, most work in literature is restricted to the characterization of AE events from different perspectives [55–57], while a simulation of complete AE waveforms cannot be achieved.

2.4. Lattice model

Lattice models are another type of DEM that are particularly suitable for AE simulations, which are promising for simulating the complete AE process [13,58]. In lattice models, a continuum is represented by a set of distributed nodes (lumped masses) interconnected by lattice elements [59–61].

- Like the particle-based DEM models, fracture-induced AE sources in lattice models are represented by the bond breakage between lumped masses. The irreversible effects of crack initiation and growth in concrete can be effectively simulated by incorporating nonlinear constitutive laws allowing the breakage of lattice elements upon reaching critical conditions [59,61].
- Wave propagation in lattice models is also simulated by solving motion equations [16,62]. Similarly to the particle-based DEM, the governing equations (motion equations) are also discrete equations assembled by bond forces between lumped masses. Nevertheless, the bond interactions between lumped masses in lattice models are alternatively established by lattice elements that can be truss [16,61], spring [63,64] or beam elements [65,66], for which the interaction laws are deduced from classical continuum mechanics; therefore, the discrete governing equations established by lattice elements are rigorously equivalent to the partial differential equations of the wave field [67,68]. As a result, the elastodynamics of wave propagation can be accurately simulated by a lattice model.

The first application of lattice modelling in AE simulation is contributed by Grabec & Petrišič [69] for the AE signals induced by tensile fracturing of polymeric materials. Subsequently, the lattice models have been applied in AE simulations in various materials [14,69–74]. Available work for lattice simulation of AE signals in fracture processes of different quasi-brittle materials was mainly contributed by Carpinteri and co-authors [12,13,58,75,76]. These efforts provide a deeper understanding of AE source mechanisms in concrete fracture process.

Nevertheless, the listed literature is still restricted to statistical characterization of AE events in the fracture processes by analyzing released energy [12], number of AE events [13] and event amplitudes [76]. Although several valuable attempts have also been made to explicitly model the fracture-induced AE waveforms [12–14,69], an accurate simulation of transient complete AE waveforms has not yet been achieved; in listed literature, the simulated AE waveforms are largely different from the experimentally measured AE signals in both time and frequency domains.

3. Methodology

This study proposes a lattice modelling approach to simulate the AE waveforms induced by tensile fracturing of concrete. The adopted lattice version was initially developed by Aydin and co-authors [77] for simulating the meso-scale mechanical behavior of concrete and reinforced concrete members [78–80]. In a previous study from the same authors [15,16], the model is modified to simulate the propagation of a transient AE wave by incorporating a proportional-integral-derivative (PID) control algorithm to minimize the dynamic noise due to external loading bias, a fracture energy regularization technique for different element sizes involved in a selected lattice grid size and a theoretic Rayleigh damping-based calculation method for simulating the attenuation of AE waves in a certain interested frequency range. An overview of the modified lattice model is described in this section.

The proposed model adopts the classical two-dimensional truss-based squared lattice network proposed by Hrennikoff [81], where a continuum is represented by a set of uniformly distributed nodes (lumped masses) interconnected by unidimensional truss elements. Fig. 1 shows a basic unit of the adopted lattice network, consisting of four lumped masses interconnected by orthogonal elements and diagonal elements. Denoting the grid size as h, the sizes of orthogonal and diagonal elements are h and $\sqrt{2}h$, respectively.

The force-strain constitutive law for truss elements is shown in Fig. 2. The elastic rigidity of orthogonal and diagonal elements (slop of the linear part of the force-strain curve under both tension and compression, as shown in Fig. 2a) is taken a same value as EA^*, where E and A^* are concrete Young's modulus and effective cross-sectional area of truss elements. The E value of truss elements is taken the same as that of concrete continuum. A^* depends on lattice grid size h and is determined by equaling the total elastic energy of a continuum to that of the equivalent lattice model under a uniform strain field [77]. In such a way, the elastic rigidity of the truss elements EA^* is strictly equal to that of represented continuum. The close-form expression of A^* and corresponding derivative process is detailed in our previous work [16]. However, it should be mentioned that the lattice models cannot precisely represent a locally isotropic continuum. Unlike an isotropic continuum, the lateral deformation of a lattice network is dependent on the lattice geometry with respect to the loading direction [82]. The inherent Poisson's ratio of the adopted 2D square truss-based lattice network varies from 0.26 (in orthogonal directions) to 0.42 (in diagonal directions) depending on the loading direction, resulting in an average value at around 0.33 [79].

Nonlinear tensile softening behavior is considered for the lattice elements in tension whereas linear elastic compressive behavior is considered for truss elements in compression (see Fig. 2a). No compression strength is defined as this study focuses on only the AE source type of tensile cracking in concrete Mode-I fracturing processes. The tensile force in the truss elements is assumed to be linear until the critical tensile strain ε_{cr} is reached, followed by a tri-linear tensile softening curve to capture the "exact" tension softening behavior of concrete (see Fig. 2a). The value of concrete cracking strain ε_{cr} is taken as a material property and determined by $\varepsilon_{cr} = \frac{f_t}{E}$, where f_t is the concrete tensile strength. To minimize the difference in fracture energy between orthogonal and diagonal elements involved in a chosen grid size, the fracture energy regularization concept [83] is implemented. Denoting the three tensile softening parameters of orthogonal elements of length $l = h$ as a_1, a_2 and a_3, the softening parameters of diagonal elements with length of $l = \sqrt{2}h$ are then divided by $\sqrt{2}$ (Fig. 2a), to assure a same stress-displacement relationship (i.e., fracture energy) for different element sizes (Fig. 2b).

It should be noted that above mentioned fracture energy of truss elements in adopted lattice model is not equal to the fracture energy as a concrete material property measured from experiments. The fracture energy of concrete is assured to be correctly simulated by the lattice model through a standard calibration procedure developed in our previous work by adjusting three softening parameters [80]. The calibration procedure is shown in Fig. 3. Specifically, we select the classical empirical model proposed by Cornelissen et al. [84] as a calibration benchmark, which was established based on a large dataset of concrete direct tension tests and provides reliable

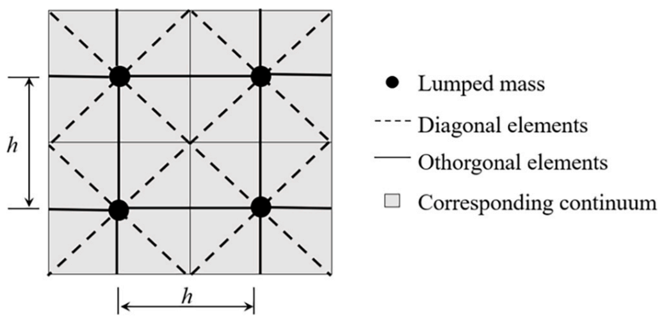

Fig. 1. A basic unit of the two-dimensional truss-based lattice network and its represented continuum.

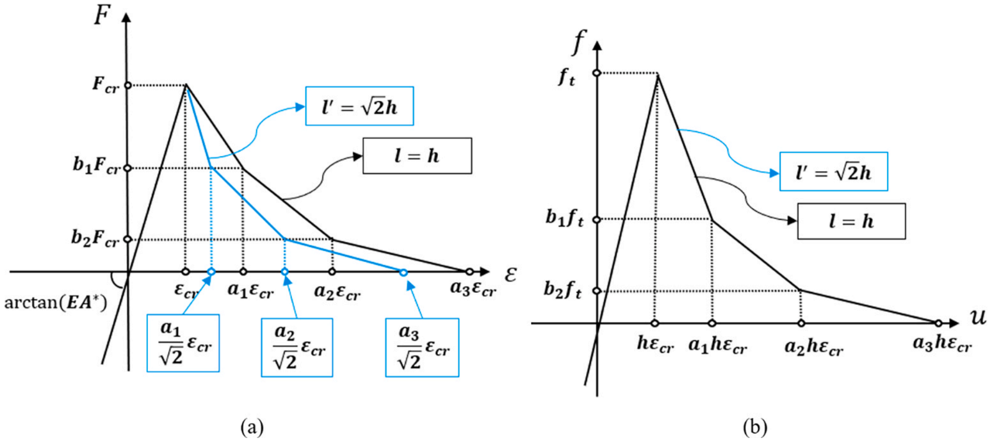

Fig. 2. Constitutive law of truss elements: (a) constitutive force-strain diagrams for different element sizes; (b) regularized stress-displacement relationships for different element sizes ($b_1 = 0.6$ and $b_2 = 0.2$).

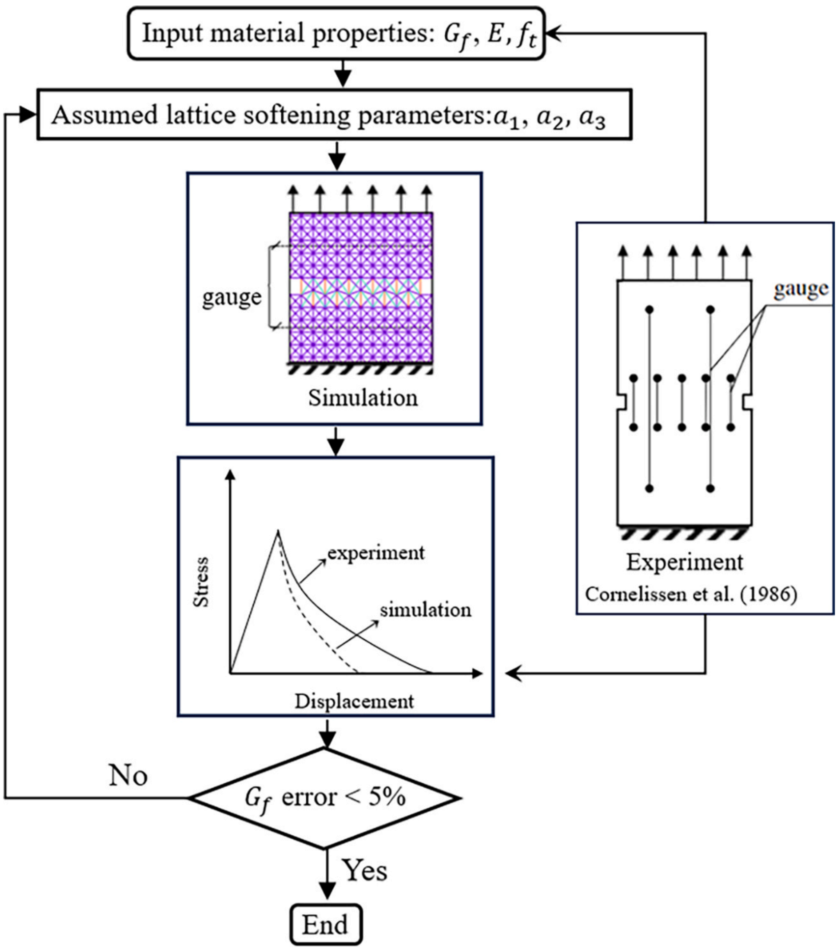

Fig. 3. Calibration procedure for the tension softening parameters [80].

empirical expressions for concrete tensile softening stress-displacement curves. By using the concrete material properties (Young's modulus, tensile strength and fracture energy) measured from our own experiments as the inputs of the Cornelissen model, we can obtain a "representative" stress-displacement curve of direct tension test as benchmark. We then use the lattice model to simulate the same direct tension test (with the same test setup) that is used for establishing the Cornelissen model. Three tensile softening parameters a_1, a_2 and a_3 of lattice elements were found such that the lattice simulation result matches the “representative” stress-average displacement response of the Cornelissen model, with three softening parameters being adjusted until the fracture energy error between lattice simulation and the “representative” test is reduced below a tolerance value (5 %). This calibration procedure is conducted prior to the formal simulation case of tested specimen which is then conducted as a blind prediction based on the calibrated parameters.

Fig. 4 shows the solution flowchart of the lattice model. The method is assembled by enforcing the second Newton’s law at every node in the model. In each time step, the force equilibrium conditions are established based on equations of motion of all the nodal masses:

$$\boldsymbol{M}\ddot{\boldsymbol{u}}(t)+\boldsymbol{C}\dot{\boldsymbol{u}}(t)+\boldsymbol{F}(t)-\boldsymbol{P}(t)=0 \tag{1}$$

where $\ddot{\boldsymbol{u}}(t)$ and $\dot{\boldsymbol{u}}(t)$ are nodal acceleration and velocity vectors, respectively. $\boldsymbol{M}$ and $\boldsymbol{C}$ are the diagonal nodal mass and damping matrices, respectively. $\boldsymbol{F}(t)$ and $\boldsymbol{P}(t)$ are the internal and external force vectors, respectively. The motion equations are solved by an explicit time integration method proposed by Chung & Lee [85].

The attenuation of the AE waves is described by the Rayleigh damping matrix $\boldsymbol{C}$ in Eq. (1) [86]:

$$\boldsymbol{C}=\alpha\boldsymbol{M}+\beta\boldsymbol{K} \tag{2}$$

where $\boldsymbol{K}$ is the stiffness matrix. α and β are the mass-proportional and stiffness-proportional Rayleigh damping coefficients, respectively. A theoretical method is established in our previous work [16] to determine suitable α and β values for modelling the attenuation of AE waves in an interested frequency range of (ω_1,ω_2):

$$\alpha(\omega_1,\omega_2)=\frac{2\left[V(\omega_2)\eta(\omega_2){\omega_1}^2-V(\omega_1)\eta(\omega_1){\omega_2}^2\right]}{{\omega_1}^2-{\omega_2}^2} \tag{3.1}$$

$$\beta(\omega_1,\omega_2)=\frac{2\left[V(\omega_1)\eta(\omega_1)-V(\omega_2)\eta(\omega_2)\right]}{{\omega_1}^2-{\omega_2}^2} \tag{3.2}$$

where the angular frequency ω with subscript $i=1,2$ denotes the lower and upper bound frequencies in an interested frequency range of (ω_1,ω_2). $V(\omega_i)$ and $\eta(\omega_i)$ denotes the velocity and frequency-dependent material damping factor, respectively, for waves of frequency ω_i.

A proportional-integral-derivative (PID) control scheme is implemented in the lattice model to exactly simulate the experimental loading conditions of $\boldsymbol{P}(t)$. The PID algorithm can be mathematically expressed as:

$$\dot{P}(t)=K_p e(t)+K_i\int_0^t e(t)\mathrm{d}t+K_d\frac{\mathrm{d}e(t)}{\mathrm{d}t} \tag{4}$$

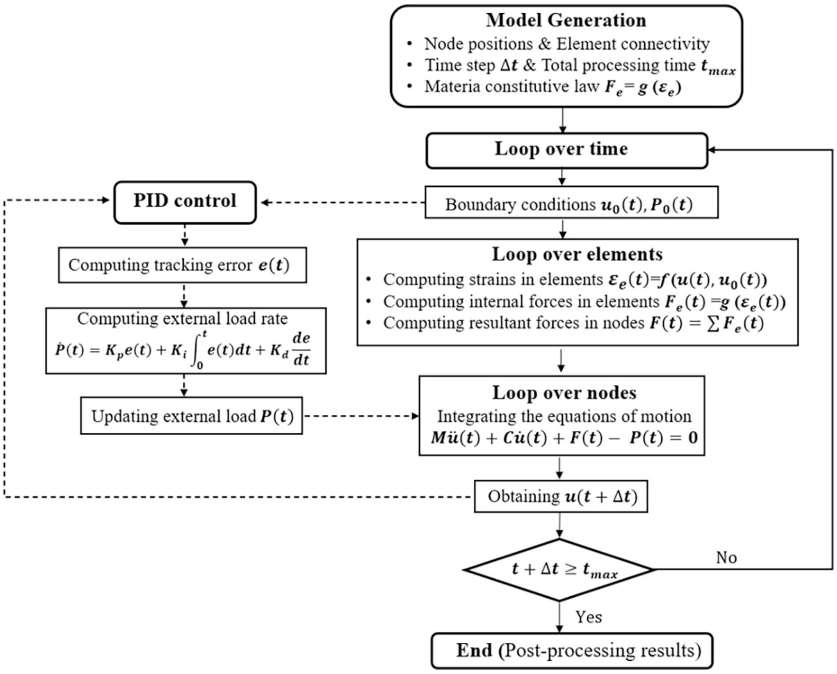

Fig. 4. Solution flowchart of the proposed lattice model.

where $\dot{P}(t)$ and $e(t)$ are the loading rate and tracking error, respectively. K_p, K_i and K_d are three PID parameters. Assuming the control variable is the velocity difference of two nodes, denoted as $\Delta v_0(t)$, and the nodal velocity difference from the computational model is $\Delta v(t)$, the error function $e(t)$ can be defined as $e(t) = \Delta v_0(t) - \Delta v(t)$. The rate of external load $\dot{P}(t)$ defined by the integro-differential equation (Eq. (4)) is solved at each step of explicit integration (Eq. (1)) to update the values of $\boldsymbol{P}(t)$. Readers are referred to the classical work of Johnson and Moradi [87] for more detail about the PID control algorithm. By adapting PID control in the explicit time integration, it is also possible to avoid high-amplitude dynamic noise signals due to loading bias between targeted and computed values of external loading $\boldsymbol{P}(t)$. More details about such effect of PID control on reducing numerical noise can be found in our previous work [16]. Readers are referred to the work of Ziegler and Nichols [88] for optimum settings of three PID parameters.

4. Experimental benchmark

The proposed modelling approach is benchmarked in this paper by a three-point bending test. The specimen geometry, material properties and experimental setup are described in this section.

4.1. Specimen and material properties

The considered beam specimen has dimensions of 550 × 150 × 40 (length × width × thickness) mm^3 with a notch of 5-mm width and 30-mm depth at mid-length. The small thickness value of 40 mm is designed to minimize the difference of wave propagation in thickness direction between the physical and corresponding numerical specimens, as the lattice model is currently restricted to 2D case. Only waves with wavelength longer than 40 mm are considered in the measurements.

The concrete has a maximum aggregate size of 8 mm and a designed strength class of C35. Material properties of the specimen are given in Table 1. The modulus of elasticity E is obtained from averaging measurements on three prism specimens (100 × 100 × 400 mm^3) from the same concrete batch. The cube compressive strength $f_{c,cube}$ and mass density ρ are obtained from averaging measurements on three cubic specimens (150 × 150 × 150 mm^3) from the same concrete batch. The cylinder compressive strength f_c is converted from measured $f_{c,cube}$ according to *fib* Model Code 2010 (MC2010) [89]. The tensile strength f_t and tensile fracture energy G_f are estimated based on the value of compressive strength f_c according to MC2010.

4.2. Experimental setup

The setup of the three-point bending test is shown in Fig. 5. Two linear variable differential transducers (LVDT) are installed across the notch on front and back surfaces (marked as LVDT1 and LVDT2 in Fig. 5) to measure the crack mouth opening displacements (CMOD). The test is conducted under CMOD control at a prescribed CMOD rate of 1×10^{-6} m/s using the average measurements from LVDT1 and LVDT2 as feedback through a PID control of the loading system. The deflection of the beam specimen is measured by another LVDT, marked as LVDT3 in Fig. 5.

Three R15a AE sensors [90] are installed on the specimen bottom surface (glued by hot melt adhesive due to lacking additional space for holder installation) to record the AE signals in the whole three-point bending test. The AE sensor layout is shown in Fig. 5b. The acquisition of AE signals is performed using the 32-channel Micro-II Express Digital AE system. The threshold and sampling rate for AE acquisition are initialized as 45 dB and 5 MHz, respectively. The hit definition parameters peak definition time (PDT), hit definition time (HDT) and hit lockout time (HLT) are set as 300, 600 and 1000 μs, respectively [91]. The waveforms corresponding to each AE hit are saved by the acquisition system for further analysis, with a 256 μs pre-trigger time and a 1.6 ms waveform recording length. Pencil-leak break (PLB) tests are conducted for each sensor before the main tests to assure sensor sensitivity and the proper settings of AE monitoring system. The definition of mentioned AE parameters is specified in Appendix A.

5. Implemented numerical model

This section describes the input parameters of built numerical model, and the output setting and postprocessing methods for numerical AE signals.

5.1. Model overview

The geometry and boundary conditions of the built numerical model are shown in Fig. 6. The grid size h is selected as 1 mm to achieve a frequency resolution up to 512.5 kHz, which is wider than the 50–400 kHz operating frequency range of experimentally used AE sensors. This estimation is based on the relationship proposed in our previous work [16] between the wave frequency resolution

Table 1
Concrete properties.

Properties (unit)	Density ρ (kg/m^3)	Compressive strength f_c (MPa)	Elastic modulus E (G Pa)	Tensile strength f_t (MPa)	Fracture energy G_f (N/m)
Values	2310	33.95	35.20	3.15	58.82

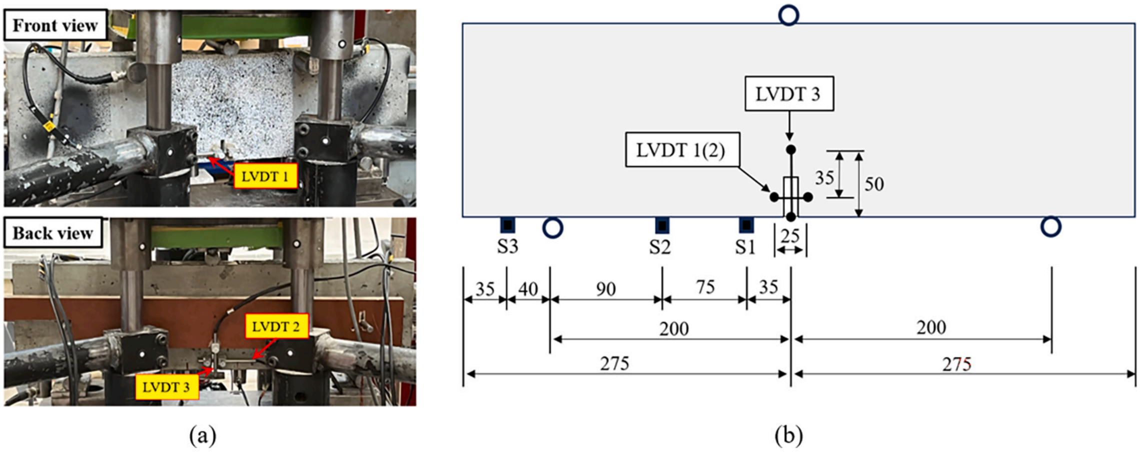

Fig. 5. Three-point bending test: (a) experimental setup; (b) schematic view of sensor locations (unit: mm).

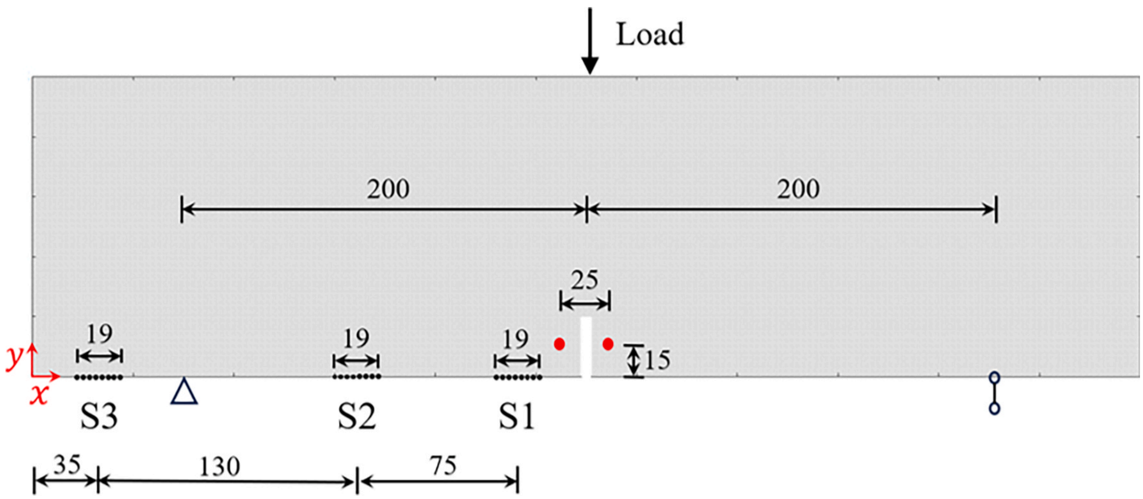

Fig. 6. Overview of numerical model (unit: mm).

and the grid size h of adopted 2D truss-based squared lattice network as:

$$f_{Ny} = \frac{V_p}{8h} \tag{5}$$

where V_p is the pressure wave velocity. f_{Ny} is the maximum wave frequency that can be achieved by a lattice grid size h without occurring of signal aliasing (called Nyquist frequency [92]).

The material properties listed in Table 1 are adopted as inputs for the numerical model. The tensile softening parameters a_1, a_2 and a_3 are calibrated as 5.5, 120 and 620, respectively, for 1 mm orthogonal lattice elements, by using the experimentally obtained E, f_t and G_f values and following the calibration procedure described in Fig. 3. The softening parameters of $\sqrt{2}$ mm diagonal elements are regularized according to Fig. 2a. It should be mentioned that concrete is modelled as a homogeneous material in this study without explicitly modelling the grain structures (namely without differentiation between mortar paste and aggregates in mesh generation). The concrete heterogeneity can influence both the cracking paths and propagation of elastic waves in the experiment. However, this study focuses on concrete tensile fracture in a three-point bending test with a relatively straight crack path, for which the influence of grain structures on cracking propagation paths is not significant. Moreover, the minimum interested pressure wavelength of 10 mm, corresponding to 400-kHz upper frequency in the 50 ∼ 400 kHz interested frequency range (see Section 4.2), is larger than the maximum aggregate size of 8 mm in the concrete beam specimen (see Section 4.1); therefore, the influence of grain structures on elastic wave propagation can be ignored. A more detailed discussion on the effect of concrete heterogeneity in AE simulation is given in Section 7.2.2.

In the notched beam specimen (Fig. 5), the wave velocities were measured as $V(\omega_1 = 2\pi \times 50\text{kHz}) = 2285$ m/s and $V(\omega_2 = 2\pi \times 400\text{kHz}) = 2349$ m/s for Rayleigh waves of 50 and 400 kHz, respectively. The material damping factors were measured as $\eta(\omega_1 = 2\pi \times$

50kHz) $= 1.05\text{Np/m}$ and $\eta(\omega_2 = 2\pi \times 400\text{kHz}) = 4.03\text{Np/m}$ for Rayleigh waves of 50 and 400 kHz central frequency, respectively. Wave attenuation testing setup and corresponding calculation procedure are detailed in our previous work [16]. Substituting the measured values of $\eta(\omega)$ and $V(\omega)$ into Eq. (3), the average Rayleigh damping coefficients covering the 50–400 kHz operating frequency range of experimentally used AE sensors are calculated as: $\alpha(2\pi \times 50\text{kHz}, 2\pi \times 400\text{kHz}) = 4574.1\text{rad/s}$ and $\beta(2\pi \times 50\text{kHz}, 2\pi \times 400\text{kHz}) = 2.28 \times 10^{-9}\,\text{s/rad}$.

The CMOD loading condition in the experiment is reproduced in the simulation by implementing the PID control algorithm. Two nodes (marked red in Fig. 6) with same coordinates of the centers of two installation holders of LVDT1(2) in the experiment (Fig. 5) are selected as controlling nodes. The rate of horizontal (x-direction) displacement difference between two controlling nodes, namely CMOD rate, is used as a PID control variable. The load is applied according to the selected PID control variable which is prescribed as the same value used in the experiment, namely the CMOD rate of $1 \times 10^{-6}\text{m/s}$. The PID constants are selected as: $K_p = 0.01, K_i = 0.01$ and $K_d = 0.05$. The parameters were selected following the procedure in the work of Ziegler and Nichols [88] to minimize spurious oscillations generated at the loading nodes, which could lead to undesired high-frequency noise in system accelerations [16]. The time step is selected as $2 \times 10^{-7}\text{s}$ in the explicit integration procedure to be consistent with the 5 MHz sampling rate used in experiments.

5.2. Postprocessing of simulated AE signals

In this section, we propose techniques for modelling the geometry and sensitivity response of AE sensors and introduce methods for extracting AE hits.

5.2.1. Sensor effect

The y-direction accelerations of bottom nodes located in the covering area of experimental AE sensors (see Fig. 6) are used to represent numerical AE signals, as AE signals received in experiments are the stress waves perpendicular to sensor surfaces. The simulated AE signals represented by nodal accelerations are continuous waveform flows in time domain. A numerical waveform flow in terms of y-direction accelerations of a node located in the center of AE sensor S1 is shown in Fig. 7, where each sudden jump in accelerations (vertical lines) is an AE hit induced by the breakage of lattice elements. A typical numerical AE waveform (the last AE hit in the loading process) is zoomed in in Fig. 7.

To compare the simulated waveforms with AE measurements, the physical geometry of the AE sensors has to be considered in interpreting the simulation results. The dimensions of experimentally used R15α AE sensor are 19 mm × 22.4 mm (diameter × height) [90] (Fig. 8a) and thus 20 bottom nodes are included in each virtual AE sensor (Fig. 8b). To account for the 2D circular geometry of AE sensor bottom surface, an area-based weight function is further assigned to each selected bottom node distributed in a 1D line, as shown in Fig. 8c. The weighted average accelerations in y direction of each selected bottom node group, denoted as $\overline{A}$, are used as a numerical representation of AE signals and calculated as follows:

$$\overline{A} = \sum_{i=1}^{n} w_i A_i \tag{6.1}$$

$$w_i = \frac{s_i}{S} = \frac{2\int_{x_i-\frac{h}{2}}^{\min\left(x_i+\frac{h}{2},\frac{D}{2}\right)} \sqrt{\left(\frac{D}{2}\right)^2 - x^2}\,dx}{\pi\left(\frac{D}{2}\right)^2} \tag{6.2}$$

where n is the number of selected nodes included in each virtual sensor ($n = 20$). w_i and A_i are the weight and y-direction accelerations of node i, respectively. s_i is the representing area of node i in the circular sensor surface (marked as blue area in Fig. 8c). S and D are

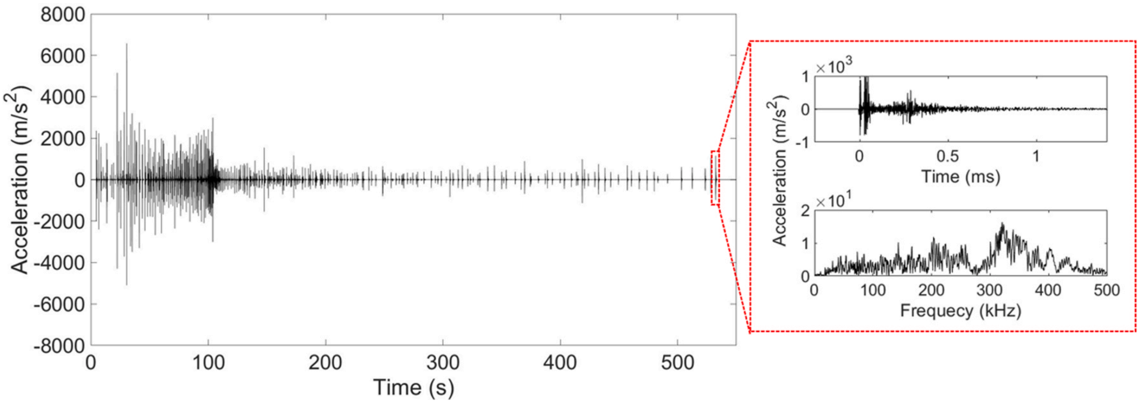

Fig. 7. Simulated AE signals (represented by y-direction nodal accelerations) received by a single node located in the center of AE sensor S1.

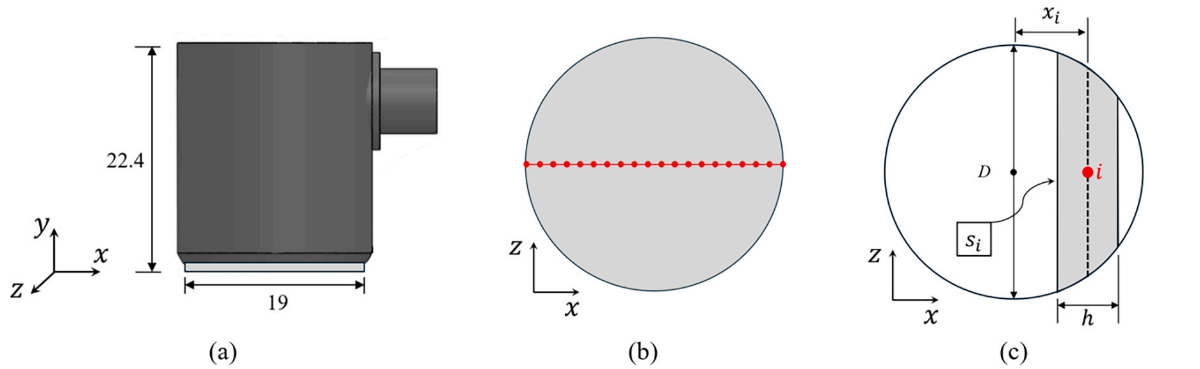

Fig. 8. Output setting of numerical AE signals: (a) dimensions of R15α AE sensor (mm), (b) selection of nodes to represent a sensor surface and (c) parameters to calculate numerical AE signals.

area and diameter of sensor bottom surface.h is the distance between two neighboring nodes (namely lattice grid size). x_i is the distance from node i to the center of sensor surface. In the main text, we only consider the geometry of the experimentally used R15α sensors. A detailed discussion on more general cases of sensor geometry effect is given in Appendix B.

In the experiments, the original elastic waves induced by concrete fracture are further transmitted into electric signals by AE sensors through piezoelectric effect. In the transformation process, the information of original elastic waves is partially lost and thus altering the waveforms, due to the frequency–response sensitivity of AE sensors, herein called "sensor effect". The frequency–response sensitivity spectrum of experimentally used R15α AE sensors is shown in Fig. 9a, which is further normalized into a sensor sensitivity function, denoted as $S(\omega)$ (Fig. 9b). The maximum function value 1 (maximum sensitivity) is achieved at the central frequency of R15α sensors and the function values are reduced for other frequency components.

For a more accurate comparison between the experimental and simulated AE signals, the "sensor effect" is applied on the numerical results. Specifically, the numerical AE waveforms considering sensor geometry $\overline{A}(\omega)$ (Eq. (6)) are further convoluted with the sensor sensitivity function $S(\omega)$ in frequency domain as:

$$A_{sensor}(\omega) = \overline{A}(\omega) \times S(\omega) \tag{7}$$

where $A_{sensor}(\omega)$ is the amplitude of numerical AE waveforms with "sensor effect".

An example of the numerical AE waveforms (the last AE hit in the loading process in Fig. 7) recorded by sensor S1 is given in Fig. 10, in terms of the accelerations of a single node in sensor center (Fig. 10a), the weighted average accelerations of multiple nodes considering sensor geometry by Eq. (6) (Fig. 10b) and the accelerations further considering sensor sensitivity by Eq. (7) (Fig. 10c). It can be observed that the waveform and frequency characteristics are both altered by the "sensor effect".

5.2.2. AE hit extraction

To isolate hit-based discrete numerical AE waveforms and to calculate corresponding numerical AE characteristic parameters, the AE waveform extraction process conducted in the AE acquisition system in experiment is applied on the simulated waveform flows (see Fig. 7). Numerical AE hits are identified in a simulated waveform flow through defining four hit definition parameters, namely threshold, PDT, HDT and HLT [91]. The numerical hit definition parameters PDT, HDT and HLT are selected as the same values used in experiments, i.e., 300, 600 and 1000 µs, respectively.

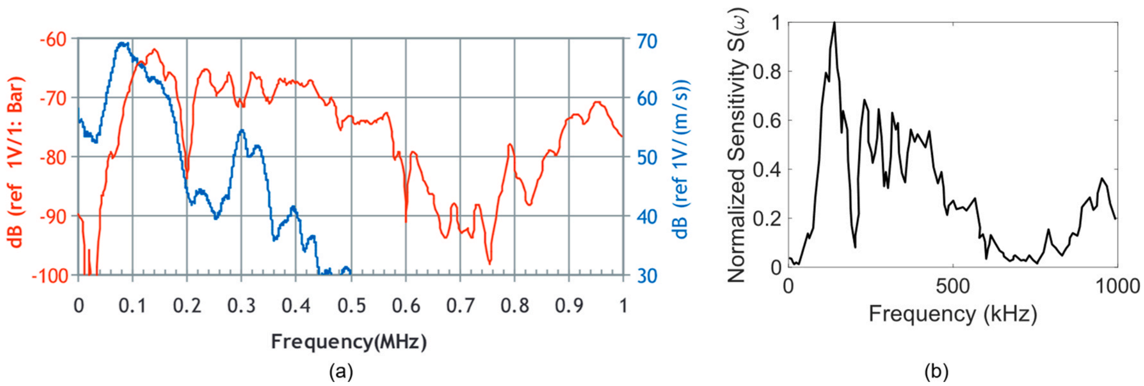

Fig. 9. "Sensor effect": (a) frequency–response sensitivity of used R15α AE (adapted from MISTRAS [90]) and (b) normalized sensor sensitivity function.

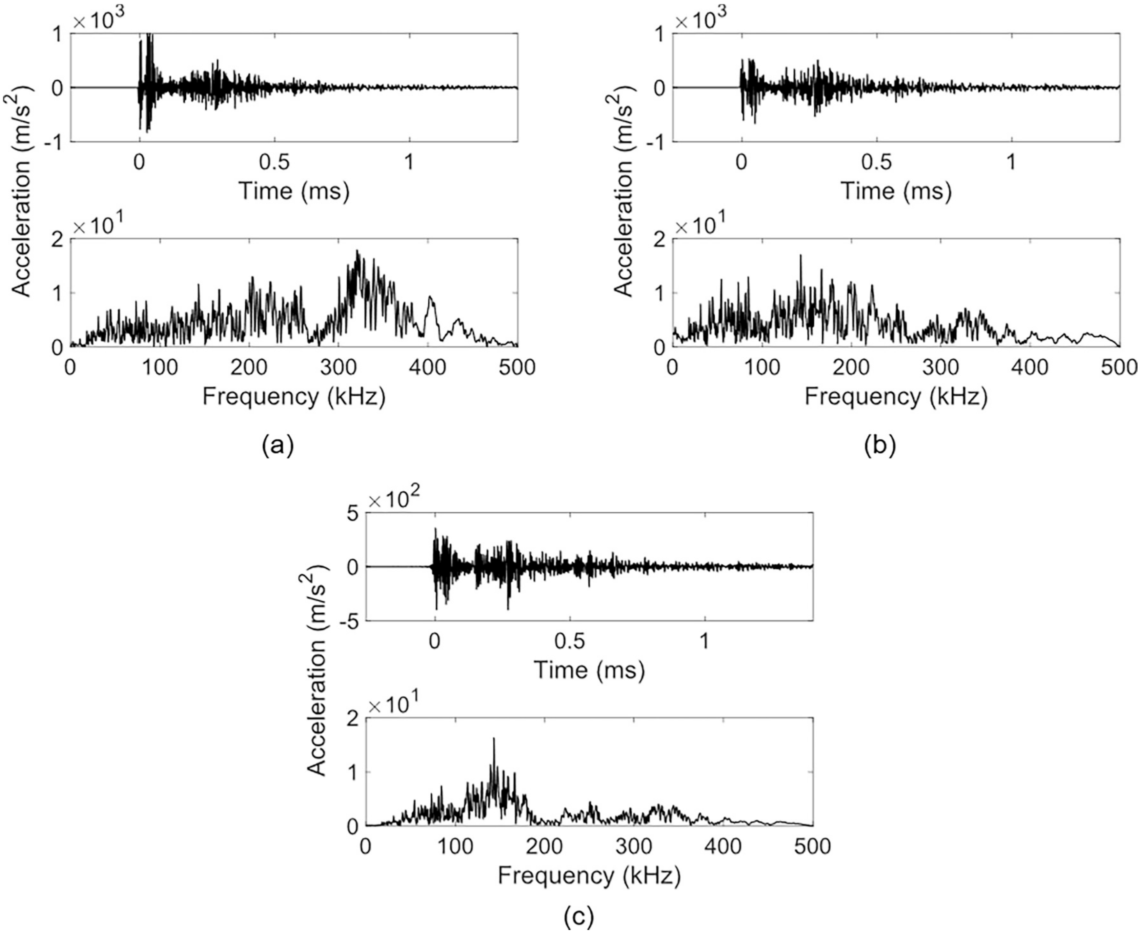

Fig. 10. Typical simulated AE signals: (a) a raw AE signal recorded by a single node; (b) a postprocessed AE signal considering sensor geometry (b) a postprocessed AE signal with complete “sensor effect”.

For the values of numerical threshold, a trial value of 0.15 m/s^2, which is chosen as twice the peak amplitude of numerical noises (i.e., the maximum value of accelerations in the absence of lattice element breakage in lattice simulations), is first applied to the continuous numerical waveform flows to isolate AE hits. The average values of peak amplitudes of isolated numerical AE hits recorded by virtual sensor S1 are calculated as: 753.5 m/s^2, 626.4 m/s^2 and 431.2 m/s^2, respectively, for the numerical AE hits represented by a single node located in sensor center, the numerical AE hits considering sensor geometry (obtained by Eq. (6)) and the numerical AE hits with completed “sensor effect” (obtained by Eq. (7)). The numerical threshold values are then evaluated by equalizing numerical and experimental ratios between threshold and average peak amplitude. Specifically, the experimental threshold and average peak amplitudes of experimental AE hits received by AE sensor S1 are 45 dB and 58.4 dB, respectively. The numerical threshold values are then

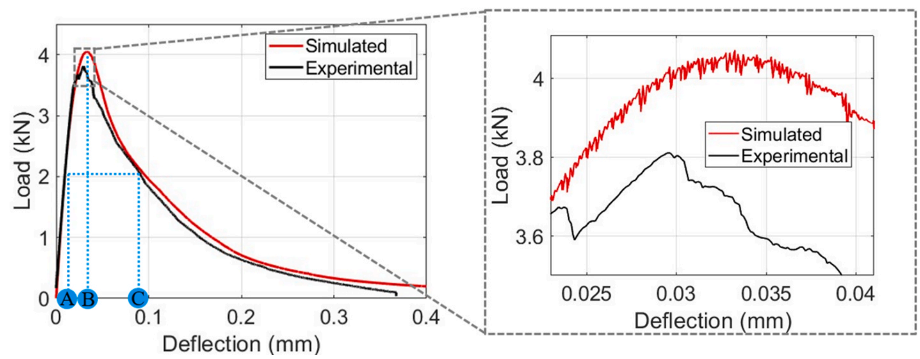

Fig. 11. Comparison between experimental and numerical load–deflection curves.

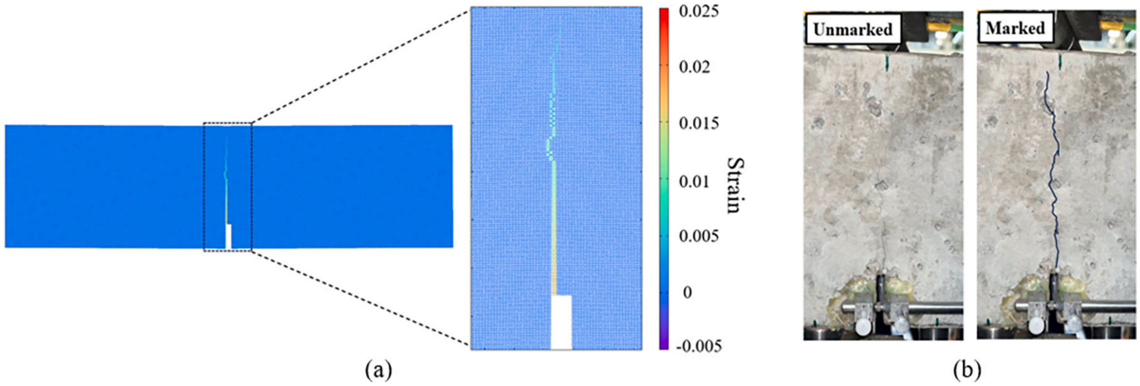

Fig. 12. Comparison in cracking patterns: (a) final numerical configuration and (b) final experimental configuration.

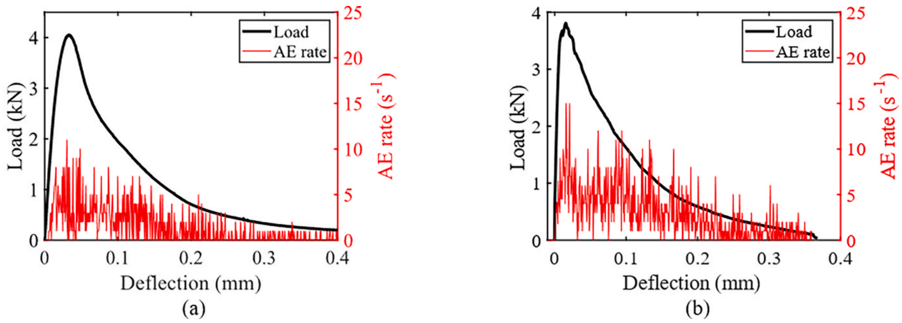

Fig. 13. AE rate received by AE/virtual sensor S1: (a) numerical results and (b) experimental results.

calculated as: $\frac{753.5\ \mathrm{m/s^2}}{(58.4-45)\mathrm{dB}} = 161.0\mathrm{m/s^2}$, $\frac{626.4\ \mathrm{m/s^2}}{(58.4-45)\mathrm{dB}} = 133.8\mathrm{m/s^2}$ and $\frac{431.2\ \mathrm{m/s^2}}{(58.4-45)\mathrm{dB}} = 92.1\mathrm{m/s^2}$, respectively, for the three numerical representation ways.

After identifying the numerical AE hits, corresponding numerical AE waveforms are isolated from the numerical waveform flows by adopting the same values of waveform recording parameters used in experiments, namely 256 μs and 1.6 ms, respectively, for pretrigger time and waveform recording length.

6. Model validation

This section reports the numerical and experimental results in different aspects, including the mechanical behavior, AE hit parameters and AE waveforms.

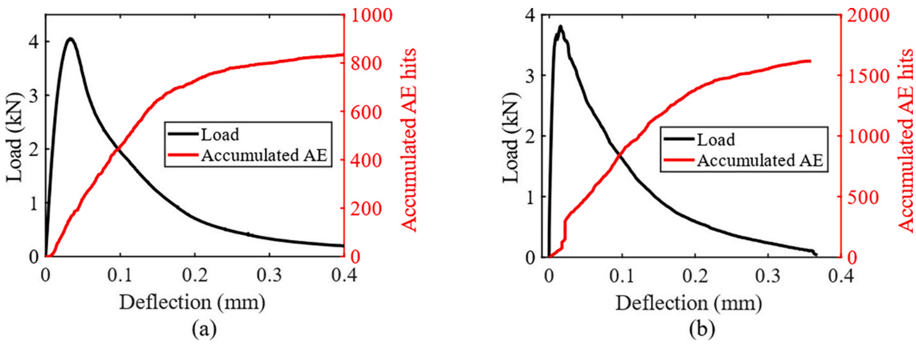

Fig. 14. Accumulated AE hits received by AE/virtual sensor S1: (a) numerical results and (b) experimental results.

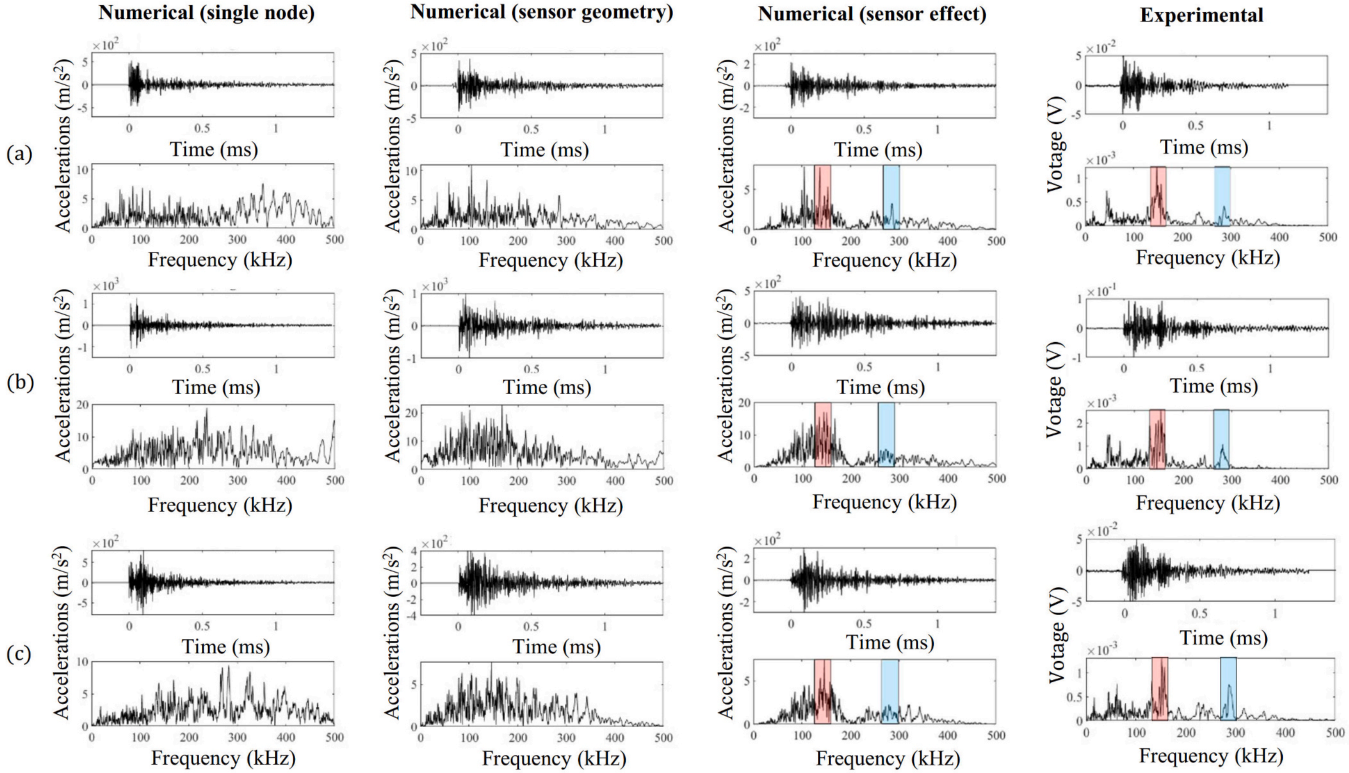

Fig. 15. Typical experimental and numerical AE waveforms received by AE/virtual sensor S1 at (a) 50% pre-peak load; (b) peak load; (c) 50% post-peak load.

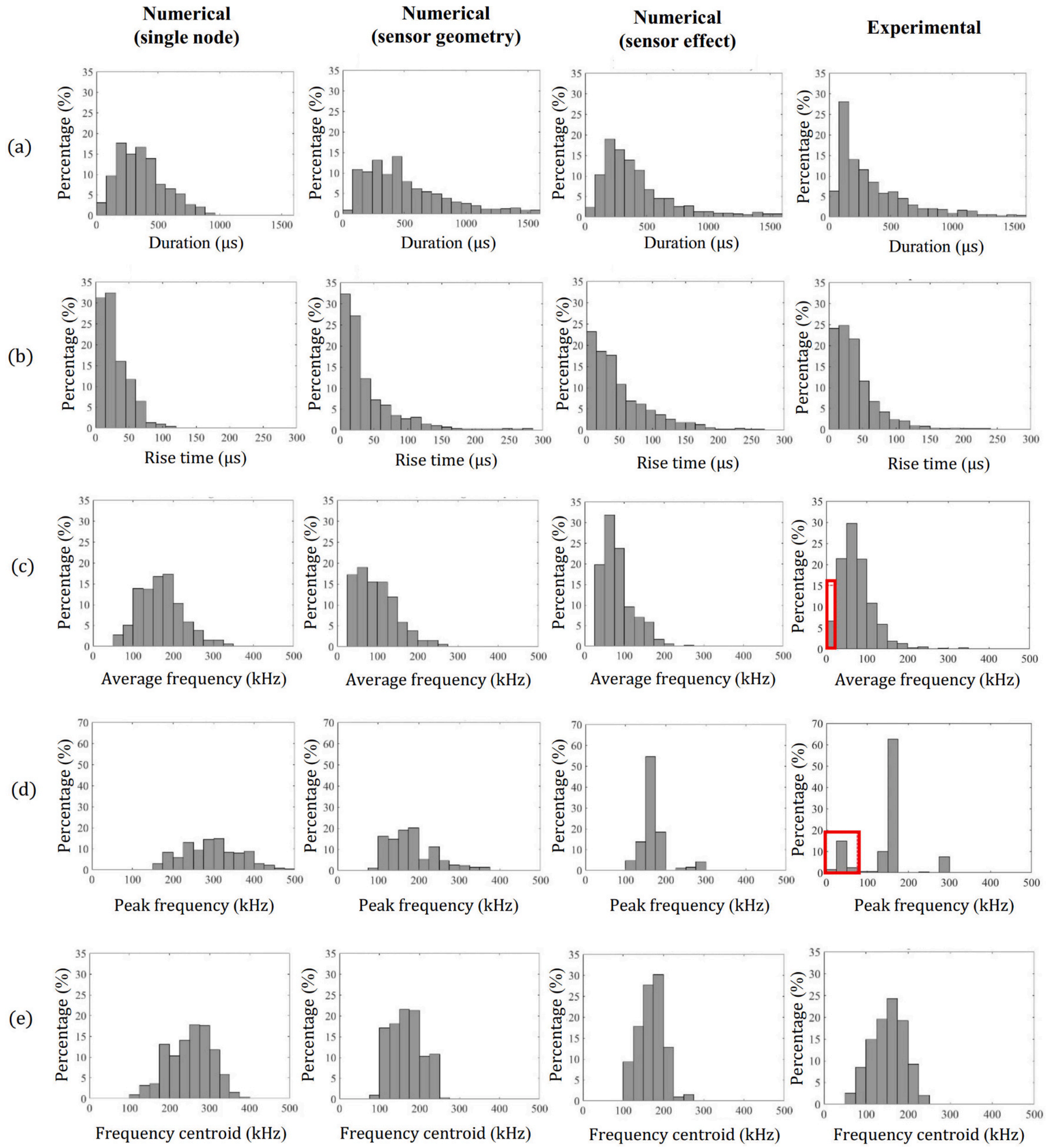

Fig. 16. Statistical comparison between experimental and numerical AE parameters received by AE/virtual sensor S1: (a) duration; (b) rise time; (c) average frequency (d) peak frequency; (e) frequency centroid.

6.1. Mechanical behavior

Fig. 11 presents the load–deflection curves of the three-point bending test obtained from both the experiment and the simulation. The numerical curve obtained by the lattice modelling is close to the experimental obtained results. The zoom-in subfigure with a gray dashed border in Fig. 11 shows the detailed mechanical behavior around peak force, where many small fluctuations can be observed in the numerical load–deflection curve, called local snap-back instability [93] or local stress drop [94]. This observation is in line with the observation from Carpinteri and co-authors [95]. Such local fluctuations are not obvious in the experimental load–deflection curve in Fig. 11, which may be attributed to the much smaller sampling rate of 10 Hz used to record loading data in our experiment (the sampling rate used in the lattice simulation is 5 MHz). Moreover, the explicit time integration solver adopted in this study for motion equations efficiently avoids the noise in a load–deflection curve in the classical lattice models [65,77,96] with the static force equilibrium being solved by a sequential linear analysis method.

The crack trajectory in the experiment and the simulation are shown in Fig. 12. Due to stress concentration, the cracks initiate at

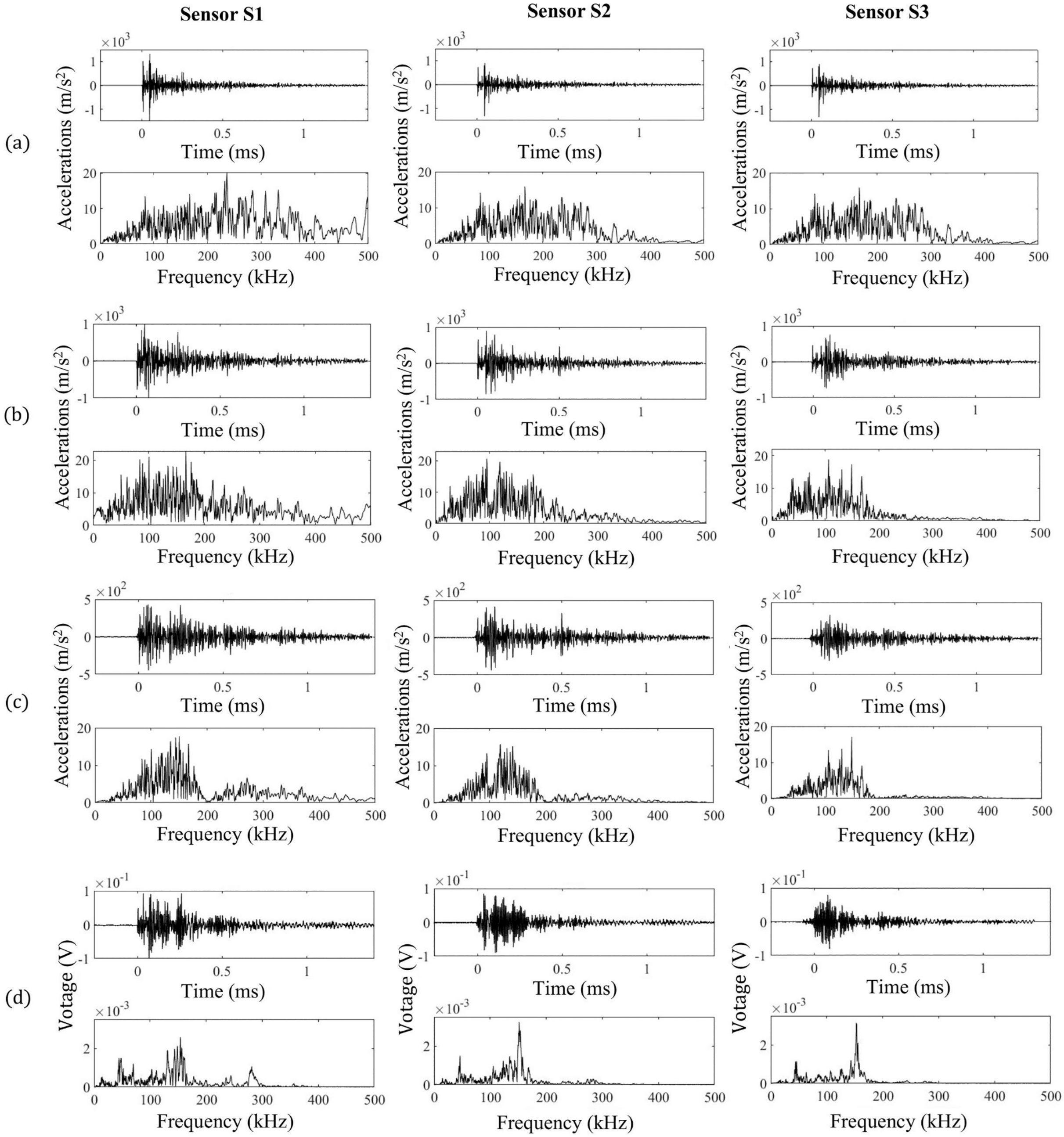

Fig. 17. Typical waveforms received by different AE sensors: (a) numerical waveforms recorded by a single node located in sensor centers; (b) numerical waveforms considering sensor geometry; (c) numerical waveforms with complete “sensor effect”; (d) experimental waveforms.

one corner of the notch both in experiment and in the lattice model. However, the numerical and experimental cracking patterns are not exactly matching. In the lower parts of the cracks corresponding to earlier loading stages, the numerical result shows a flat crack path whereas a kinked crack is observed in the experimental result. Such a kinked cracking trajectory in the experiment can be attributed to the heterogeneity of concrete material, i.e., cracks mainly developing along the mortar paste between randomly distributed aggregates in experiment.

Nevertheless, the numerical and experimental results both show an irregular curved crack trajectory in upper parts corresponding to later loading stages. Such a curved cracking path in numerical results can be attributed to the large displacements occurring in certain loading stages. Specifically, large displacements are accounted for naturally in the proposed lattice model by adopting a Lagrangian-type solver proposed by Chung & Lee [85] for solving motion equations. The iterative operation is carried out by means of coordinate updating, i.e., the deformed coordinates of the mesh after each iteration are used as the new starting coordinates, to simulate the actual deformation more realistically. Moreover, to account for the effect of stress states on local cracking behavior, we set a same value of elastic rigidity EA^* and thus slightly different values of elastic stiffness EA^*/l for orthogonal and diagonal elements with different sizes l (see Section 3). In this way, when large displacements occurring in certain stress states in the loading process, strains are localized in the weaker diagonal elements and then the cracking propagation direction is deviated, although without considering the concrete heterogeneity (differentiation between mortar paste and aggregates) in mesh generation.

6.2. AE hits

Following the procedure discussed in Section 5.2.2, the AE hits and their distribution in the loading process, including AE rate (herein defined as the number of AE hits per second) and accumulated AE hit number are calculated from the simulation. The analyses are based on the AE signals received by sensor S1 which has the closest distance to the crack (see Fig. 6). The AE rate and accumulated AE hits are shown in Figs. 13 and 14, respectively. A good agreement is observed between the experimental and numerical results. High AE rates and thus rapid increasement in accumulated AE hit numbers occur in the stage of 0.01 ∼ 0.15 mm mid-span deflection, the AE activities are then gradually suppressed in later pos-peak loading stage. However, it should be noted that there is an obvious difference between numerical and experimental AE hits at around peak load: a spasmodic AE behavior can be observed in the experimental results in terms of an obvious jump in the number of AE events at the peak load (see Fig. 14b), which can be attributed to diffuse damage resulting from concrete material heterogeneity. A more detailed discussion about the effect of concrete heterogeneity on AE modelling is given Section 7.2.2.

The total number of experimental and numerical AE hits received by AE/virtual sensor S1 are 1617 and 833, respectively. The 2D lattice model produced a smaller number of numerical AE hits because the sizes of microcracks (AE sources) in the model is limited by the size of the lattice elements. In addition, current version of the proposed lattice model cannot consider other AE sources other than tensile fracturing (e.g., friction between crack surfaces). A more detailed discussion on this is given in Section 7.1. It should be mentioned that it is possible to generate more numerical AE hits by using a smaller lattice grid size, due to the dependence of broken lattice element number on the lattice discretization level. The lattice mesh dependence for elastic wave propagation simulation is detailed in our previous work [16]. Limited by the size of paper, the influence of lattice discretization level on AE sources and their evolution in fracturing process will be reported in a following-up study.

6.3. AE waveforms

A selection of typical numerical and experimental AE waveforms obtained by sensor S1 are shown in Fig. 15. Three presented signals are randomly selected at around 50 % pre-peak load, peak load and 50 % post-peak load (corresponding to blue circles A, B and C marked in Fig. 11), respectively. To illustrate the influence from the geometry and frequency–response sensitivity of AE sensors, for each numerical signal, its original waveform recorded by a single node located in sensor centre, the waveform obtained by Eq. (6) considering sensor geometry and the waveform obtained by Eq. (7) considering complete “sensor effect” are all presented.

It can be observed that the numerical AE signals recorded by a single node (first column in Fig. 15) have shorter duration and more high-frequency components. After considering the geometry of AE sensors, the numerical and experimental AE waveforms show high similarity. In time domain, the signals show high amplitudes from 0 to around 0.2 ms and then are gradually attenuated in amplitudes. In frequency domain, compared to the numerical AE signals only considering sensor geometry (second column in Fig. 15), the numerical signals further accounting for the frequency response of sensor (third column in Fig. 15) are closer to the experimental AE signals. The numerical waveforms with complete “sensor effect” and experimental waveforms both show a main frequency peak at around 150 kHz (marked red in Fig. 15) and secondary peak at around 300 kHz (marked blue in Fig. 15).

It is meaningless to conduct a point-to-point comparison between numerical and experimental signals, because even the experimental AE signals show large discrepancy in waveforms from each other, as shown in Fig. 15. A statistical comparison is then conducted between numerical and experimental AE signals, in terms of typical AE characteristic parameters. The definition of mentioned AE parameters is specified in Appendix A.

The distribution of AE hit parameters from both simulation and experiments are summarized in Fig. 16. For the duration and rise time (Fig. 16a–b), the experimental and numerical signals show similar statistical distributions. The response of single node (first column in Fig. 16) shows shorter duration and rise time in comparison with the numerical results considering sensor geometry and the experimental results. For the frequency characteristic parameters (Fig. 16c–e), larger difference can be observed between the numerical results using the three different representation methods. The statistical results of the response of a single node (first column in Fig. 16) show a wider distribution along frequencies. After considering the sensor geometry (second column in Fig. 16) and sensor frequency response (third column in Fig. 16), the distributions of numerical waveforms are closer to those of experimental waveforms: the distributions of average frequency, peak frequency and frequency centroid are mainly concentrated at around 40–100 kHz, 150 kHz and 100–220 kHz, respectively.

It should be noted that there is an obvious difference in average frequency and peak frequency between experimental and numerical results. About 20 % of the experimental signals have average and peak frequencies in the range of 0 ∼ 40 and 0 ∼ 75 kHz (marked by red dashed boxes in Fig. 16c and d), respectively, while such low-frequency signals are not observed in numerical simulations. A detailed discussion on possible reasons for this discrepancy is given in section 7.1.

6.4. Spatial variation of AE parameters

To evaluate the ability of the developed lattice model in simulating the attenuation of AE signals propagating in concrete, a comparison is conducted between AE signals received by three AE/virtual sensors (S1, S2 and S3 in Fig. 5) with various distances to cracking sources. AE signals received by different AE sensors are clustered into AE events according to their arrival time differences. AE signals with arrival time differences less than 58.5 μs ($\Delta t_{max} = \frac{\Delta d_{max}}{V_p} = \frac{240\text{mm}}{4100\text{ m/s}} = 58.5\mu\text{s}$, where Δd_{max} is the maximum sensor spacing distance) are considered from a same AE source and classified into a same AE event. For experimental results, the AE events only received by one or two sensors are discarded and those can be received by all the three AE sensors are used for analyses in this section. The total number of experimental AE events kept for analyses are 1152.

Numerical and experimental waveforms received by three AE sensors from a typical AE event randomly selected at around the peak load is shown in Fig. 17. Similarly, for numerical results, we show the original waveforms recorded by a single node located in sensor centre (Fig. 17a), the waveforms obtained by Eq. (6) considering sensor geometry (Fig. 17b) and the waveforms obtained by Eq. (7) considering complete "sensor effect" (Fig. 17c). With increasing the distance from sensor to cracking source, a decreasing trend is observed in both the time-domain peak amplitudes and the amplitudes of high-frequency components (200 ~ 500 kHz) in frequency domain for all three different numerical representation choices.

Statistical analyses are conducted considering the changes in distributions of peak amplitudes and peak frequency of AE signals received by sensors S1, S2 and S3. Fig. 18 shows the statistical change in peak amplitudes, where the peak amplitudes of sensors S2 and S3 are both normalized relative to those of S1 in dB as:

$$A_k^{(normalized)} = 20\log\left(\frac{A_k}{A_1}\right) \tag{8}$$

where $A_k^{(normalized)}$ and A_k are the normalized and original peak amplitudes for an AE event received by sensor k ($k = 2, 3$). A_1 the original peak amplitudes for an AE event received by sensor S1. It can be observed that the statistical distributions of numerical and experimental results are similar and there is no large difference between the numerical results using three different representation methods. The drop in normalized peak amplitudes relative sensor S1 of signals received by sensor S2 and S3 are mainly distributed in the range of 0 ~ 6 and 3 ~ 12 dB, respectively, for both the numerical and experimental AE signals.

The statistical distributions of peak frequency are shown in Fig. 19. Compared to the above little influence of "sensor effect" on time-domain peak amplitudes, the geometry and frequency response of sensor show large effect on the attenuation characteristics of signal peak frequency. The numerical AE signals represented by a single node (Fig. 19a) show a larger spreaded discrepancy from the experimental signals. After accounting for the sensor geometry, the peak frequencies of all three sensors are narrowed to the range of 100 ~ 200 kHz (Fig. 19b). By further considering the frequency response of sensor (Fig. 19c), the statistical distribution of numerical AE signals is much closer to that of experimental signals (Fig. 19d): the percentages of AE signals with peak frequency concentrated at around 150 kHz slightly increase with increasing the distance from sensor to sources, while the percentages of signals with higher peak frequency (at around 300 kHz marked in blue in Fig. 19c-d) are significantly reduced with increasing the sensor-to-source distance. Additionally, there is an obvious difference in peak frequency distribution between numerical and experimental AE signals for all the three sensors: the low-frequency signals with peak frequency at around 50 kHz (marked in red in Fig. 19c-d) in experimental results do not exist in the simulation. Corresponding explanations are given in section 7.1.

7. Discussions

This study presents a lattice modelling approach to explicitly simulate the complete AE waveforms induced by concrete tensile fracturing. To the best knowledge of the authors, to date, the proposed method is the first model in literature that can explicitly simulate both the mechanical responses of concrete fracture processes, and the AE waveforms measured during the fracturing processes with one model and with relatively simple modelling and calibrating process. The proposed model has distinguished advantages among available AE modelling methods. It relies only on the concrete mechanical properties with clear physical meanings as model inputs; AE signals are automatically generated as a direct result of concrete fracturing processes and do not require additional inputs for the AE phenomenon itself. Compared to traditional continuum-based analytical models and numerical FEM, the proposed model does not need additional assumptions (external inputs) for the description of AE sources. With respect to other DEM, the proposed model can explicitly simulate the transient elastodynamic effects of elastic wave propagation and attenuation triggered by element breakage, and thus the complete fracture-induced AE waveforms.

To date, limited evidence has been given in literature showing how AE signals are linked to the physical fracturing processes of concrete. There are two main AE source types involved in concrete fracturing processes, tensile cracking at fracturing process zone (crack tip) and friction along existing cracking surfaces. The proposed lattice model is promising to uncover AE sources mechanisms induced by concrete tensile fracturing. Further study will focus on the establishment of quantitative relationships between the concrete tensile fracture behavior (e.g., fracturing size, fracturing parameters and concrete material properties) and typical parameters of induced AE signals by parametric analyses using the developed model.

Additionally, the fracturing phenomena of crack nucleation, propagation and coalescence to form macroscopic fracture can be reflected in lattice modelling through element breakage and the accumulation of broken elements [68]. Therefore, the developed model also has great potential to investigate the evolution of AE sources and resultant change in AE parameters in different fracturing stages, thus towards developing reliable AE indicators for concrete structural damage states. Furthermore, the developed lattice model can be of interest for the full-waveform modelling of fracture-induced AE signals in other brittle and quasi-brittle materials, e.g., rocks.

The proposed model, however, has its limitations. In the following, we discuss the model limitations and possible improvements.

7.1. Explanations for the difference in frequency characteristics between experimental and numerical AE signals

As can be seen in Figs. 16c–d and 19c, there are differences in the average and peak frequencies between numerical and experimental AE signals. The experimental results include around 20 % AE signals with low average and peak frequencies, while such low-frequency signals are not observed in numerical results. Possible explanations for this discrepancy are given in the following.

In plain concrete, AE signals are mainly from two source types, tensile cracking (Mode-I fracture) and stick-sliding friction along existing crack surfaces [4]. AE signals from these two mechanisms show different waveform characteristics. It is well-known that the AE signals from tensile cracking are characterized by higher average frequency and shorter rise time. The AE signals from friction are characterized by lower average frequency and longer rise time [5]. This explanation is in line with the observation in the research of Zhang et al. [4], in which it was proposed that the cracking-induced AE signals have peak frequency values higher than 70 kHz, while friction induced AE signals may have peak frequency lower than 70 kHz. As shown in Fig. 12, the surface cracks in the three-point bending test are not perfectly straight involving sliding along the crack surfaces. The low-frequency signals observed in the experiments may be caused by the friction along crack surfaces. There is no low-frequency AE signal from stick-sliding friction in the simulation, because only tensile failure mechanisms are considered in the current lattice modelling framework. In addition, parts of the experimental low-frequency AE signals can be attributed to the noises from the loading device.

7.2. Limitations of current research and recommendations for future study

The limitations of current research and corresponding recommendations for a future study are discussed in this section.

7.2.1. Influence of existed cracks on wave propagation

In the proposed lattice model, the implemented numerical Rayleigh damping can simulate the intrinsic wave attenuation of the undamaged concrete, while the attenuation and reflection of AE waveforms caused by cracks cannot be correctly simulated. Specifically, to ensure the reduction of the mechanical properties, the stiffness of the cracked elements must be reduced in the lattice model. However, following the Rayleigh damping formulation (see Eq. (2)), this reduction of stiffness will lead to a lower of damping, as the damping values of nodes linked by a broken element are reduced when its stiffness degrades. On the contrary, in reality, the damping value at a cracked region shall increase towards an infinitely large value (the cracking surfaces can be seen as additional boundaries). This challenge can be resolved by two possible solutions. One option is to remove the broken elements to create cracking boundaries in each calculation step. The other is to set increasing damping values for the nodes linked by broken elements; here, as the damping values of cracked elements will not be linearly linked to the stiffness of the elements, a dedicate calibration of the damping effect of cracked concrete with respect to the crack width, wave propagation angle and polarization shall be carried out [97].

7.2.2. Concrete heterogeneity

In microscopic level, concrete is a highly heterogeneous material. The heterogeneity may influence both source mechanisms and AE wave propagation: the AE sources from the fracture of mortar, aggregates or their interface may be different; the presence of aggregates or pores in concrete leads to wave scattering of AE signals. In this study, the concrete is modelled as homogeneous material without considering the differentiation between mortar paste and aggregates in mesh generation. In a future study, the influence of concrete heterogeneity on simulated AE signals should be investigated. In lattice modelling, the concrete material heterogeneity can be simulated by either applying random distribution of element material parameters, e.g., fracture energy [12] or by adopting a random lattice mesh (i.e., perturbing lattice grids with small random displacements or random angles [79]). The material disorder has been considered in classical lattice modelling work and is seen as an essential part to simulate an AE test [12–14].

7.2.3. Limitation of 2D simulation

The developed lattice model is currently restricted to 2D simulation and thus cannot simulate the propagation of AE waves and the fracturing process inside concrete in 3D. To ensure enough temporal and spatial sampling rates of simulated AE signals, small values were used for both the mesh size and time step in the simulation, leading to more computational resources. Although the vectorization and parallelization computing techniques have been applied in the lattice modelling platform, the computation time is still around 10 days for the simulation case presented in this study even using a high-performance workstation.

In a future study, a more efficient 3D lattice model is necessary for a better simulation of wave propagation and internal fracturing processes in real structures. One possible solution is to use varied time steps in the explicit integration procedure, adopting a much larger time step when no lattice element is broken. The second possible solution is to combine the lattice model with finite element methods (i.e., combined finite-discrete element method [42]); the possible cracking region is still modelled by lattice elements and the remaining undamaged parts can be modelled by elastic finite elements.

8. Conclusions

To establish a clear relationship between the AE signals measured during the fracturing processes and the physical sources that induces the signals, it is ideal to establish a forward model that can explicitly model the fracturing processes of concrete, the propagation of AE waves and the sensor effect. This study develops a numerical method to achieve the completed waveform simulation of fracture-induced AE in the framework of lattice modelling approach by extending an already developed lattice model dedicated for concrete fracturing simulation with additional techniques that can accurately simulate the propagation and attenuation of elastic

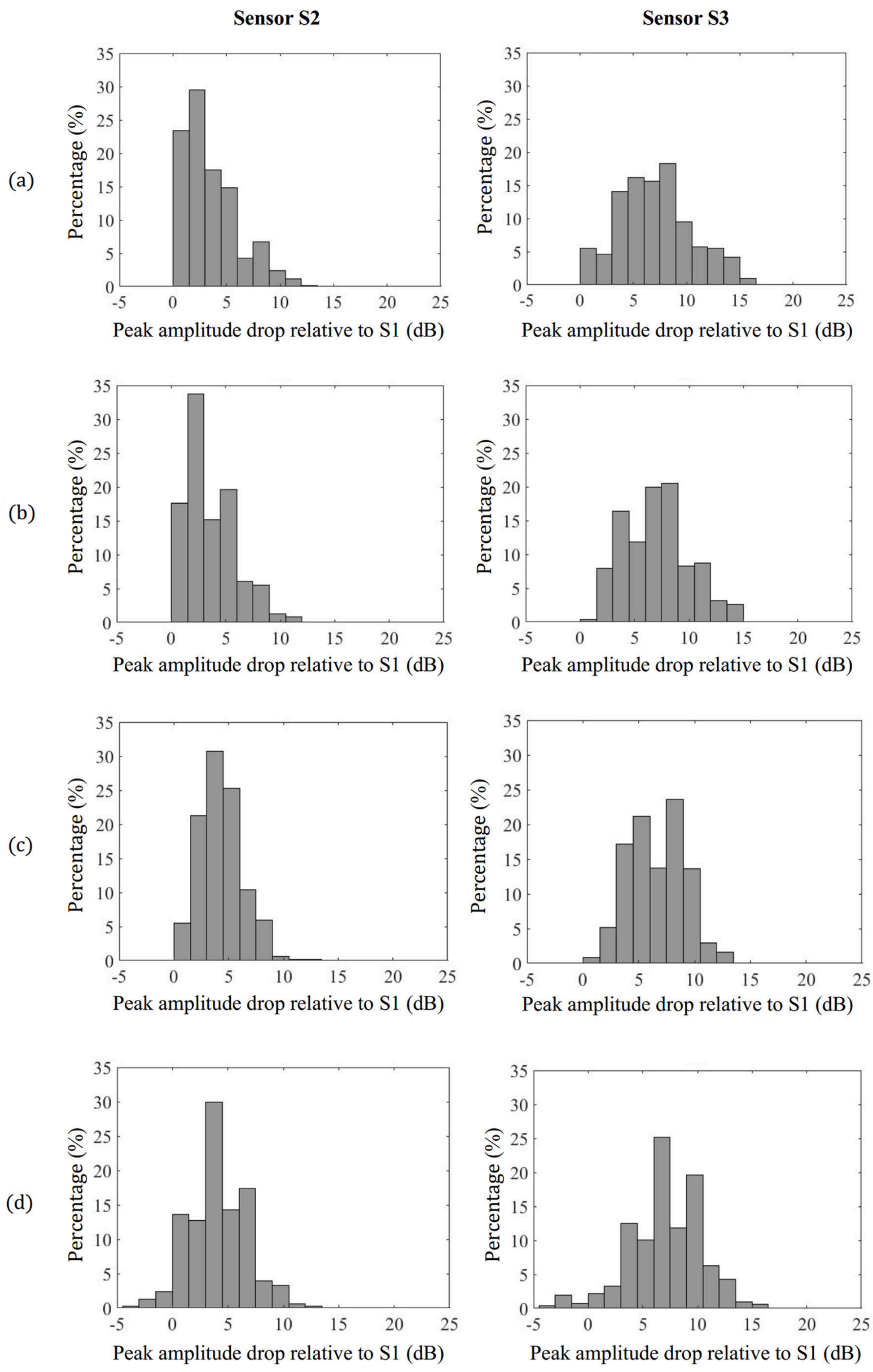

Fig. 18. Distribution of AE peak amplitudes relative to sensor S1: (a) numerical results recorded by a single node located in sensor centers; (b) numerical results considering sensor geometry; (c) numerical results with complete "sensor effect"; (d) experimental results.

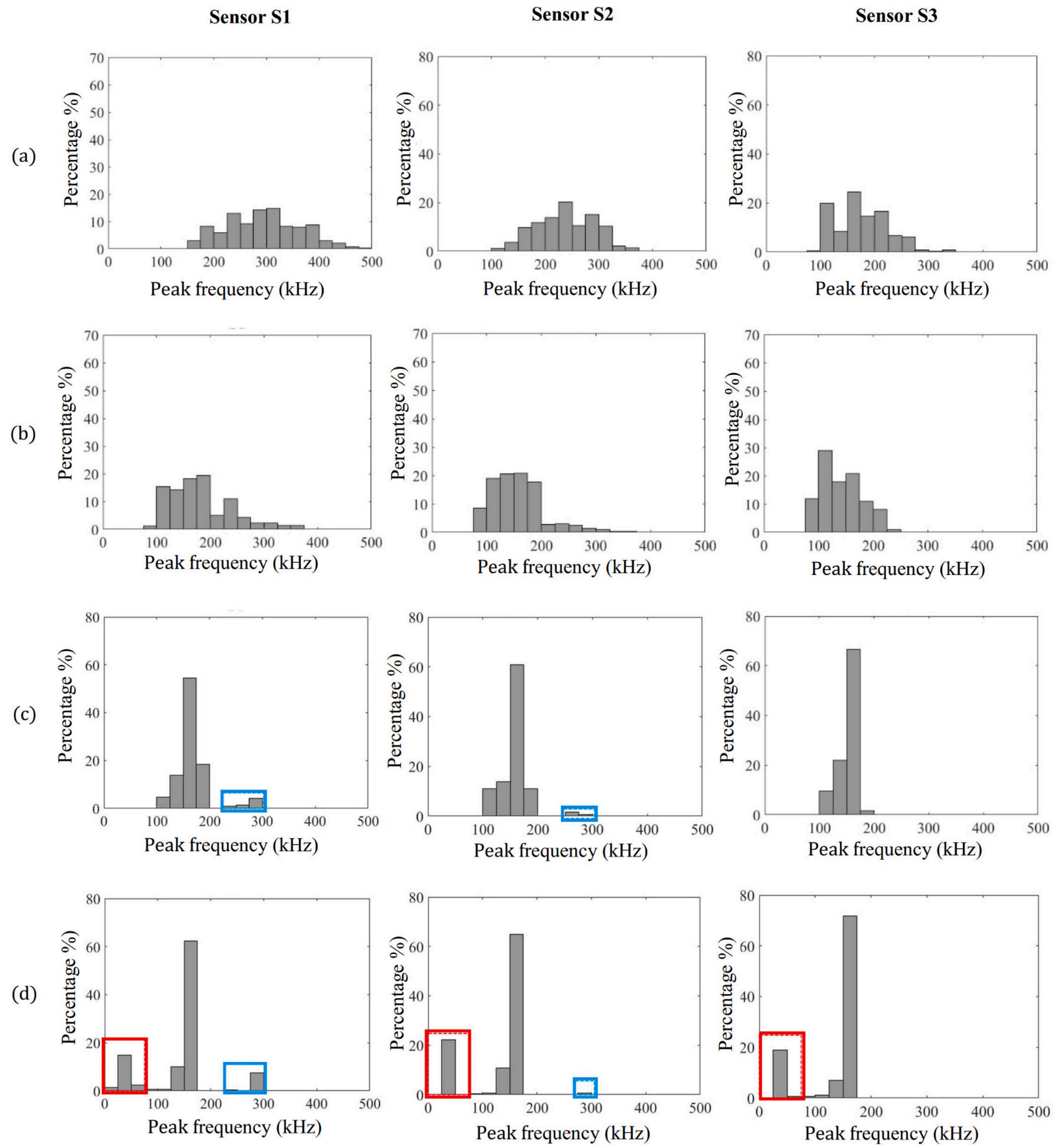

Fig. 19. Distribution of peak frequency of signals received by different AE sensors: (a) numerical results recorded by a single node located in sensor centers; (b) numerical results considering sensor geometry; (c) numerical results with complete "sensor effect"; (d) experimental results.

waves as well as the sensor effect.

The feasibility of the proposed model for tensile fracture-induced AE waveform simulation has been demonstrated through a comparison with experimentally obtained AE signals. The simulated AE waveforms show a high degree of similarity statistically to the measured AE signals from a three-point-bending test in terms of typical AE parameters. The proposed lattice model is of significance for a fundamental understanding of AE source mechanisms in concrete fracturing processes and for addressing current challenges faced by the AE technique.

While the focus of this study is to propose a novel lattice approach for simulating the AE waveforms from concrete tensile cracking (Mode-I fracture), the potential applicability of the methodology to other possible AE source types involved in concrete fracture processes, e.g., stick-sliding friction between cracking surfaces, could be explored in future investigations. It also remains unclear how the mesh size in the proposed lattice model affects simulated AE signals, and how that means physically. Moreover, this paper focuses on a statistical comparison between experimentally and numerically obtained AE waveforms without discussing the evolution trends of AE signals during concrete fracturing processes. These aspects will be addressed in a following-up study.

CRediT authorship contribution statement

Yubao Zhou: Writing – review & editing, Writing – original draft, Visualization, Software, Resources, Methodology, Investigation, Funding acquisition, Formal analysis, Data curation, Conceptualization. **Beyazit Bestami Aydin:** Writing – review & editing, Validation, Software, Methodology, Investigation. **Fengqiao Zhang:** Supervision. **Max A.N. Hendriks:** Validation, Supervision, Resources, Project administration, Methodology, Funding acquisition. **Yuguang Yang:** Writing – review & editing, Validation, Supervision, Resources, Project administration, Funding acquisition, Conceptualization.

Declaration of competing interest

The authors declare that they have no known competing financial interests or personal relationships that could have appeared to influence the work reported in this paper.

Acknowledgment

We acknowledge the valuable discussion and advice on the influence of AE sensor geometry to its response sensitivity from Prof. Dimitris Aggelis at Vrije Universiteit Brussel.

Appendix

A. Definition of typical AE parameters

As many AE parameters are mentioned and analyzed in this paper, the definition of typical AE parameters used in this paper is briefly described in this appendix. AE parameters can be mainly distinguished into three categories, including hit definition parameters, characteristic parameters and hit-based waveform recording parameters.

The hit definition parameters are used to extract burst AE signals (AE hits) from a measured continuous waveform flow. Threshold, peak definition time (PDT), hit definition time (HDT) and hit lockout time (HLT) are four hit definition parameters. As illustrated in Fig. A1a, the threshold specifies the starting time of an AE hit. The PDT is the period that allows to determine the peak amplitude of an AE hit. The HDT is the maximum allowed period between threshold crossing in an AE hit: the hit has ended if no further threshold crossing occurs during the HDT. The HLT is the minimum period for detecting a new hit after the end of previous hits, to avoid falsely detecting the reflected or delayed waves as independent AE hits.

After identifying an AE hit, its characteristic parameters can be calculated. Typical time-domain characteristic parameters are illustrated in Fig. A1a. Duration is the period between the first and last threshold crossing. Rise time is the period between the first threshold crossing and the peak amplitude. AE count is the number of signal oscillations crossing the threshold. The ratio between count and duration is defined as average frequency. As illustrated in Fig. A1b, peak frequency and frequency centroid are two main frequency-domain characteristic parameters. The peak frequency is a frequency value corresponding to the maximum energy spectrum point. The frequency centroid is a frequency value that divides the frequency spectrum into two equal areas.

AE waveforms can be recorded in an AE acquisition system in two ways: either recording the complete continuous waveform flow or recording discrete waveforms based on AE hits. The second method is commonly used due to less need of storage space. Pre-trigger time and waveform recording length are two main parameters to recover AE waveforms from identified hits, as shown in Fig. A1b. The pre-trigger time is the period before the first threshold-level crossing. The waveform recording length is the total recording period for a waveform. It should be mentioned that the parameters mentioned herein are only parts of AE parameters. The definition of complete AE parameters can be found in the book [98].

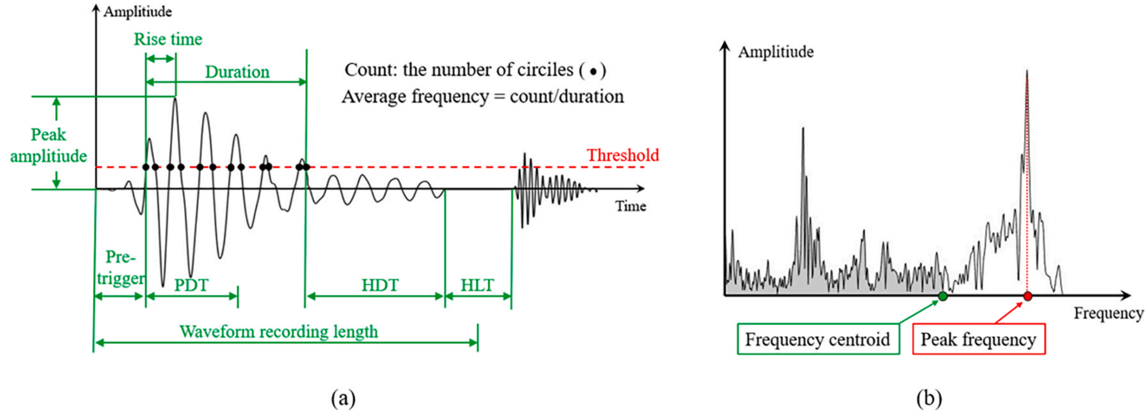

Fig. A1. Illustration of typical AE parameters: (a) time domain; (b) frequency domain.

B. Influence of sensor geometry on simulated AE signals

In the main text, we have considered the influence of the physical geometry of sensors in the presented simulation case. Nevertheless, the analyses account only for one geometry of a specific sensor type, namely R15α AE sensors with a circular surface of 19 mm diameter. In this appendix, we analyze the relationship between the diameter of sensor surface D (see Fig. 8) and typical parameters of simulated AE signals in lattice modelling. We adopt the same numerical case in the main text (see Section 5.1) for analyses. The first numerical AE signal in the loading process of the three-point bending test is considered. The analyses are based on a combination of nodes with a central coordinate of (250 mm, 0) (namely S1 in Fig. 6). The weighted average accelerations in y direction calculated by Eq. (6) are used to account for the effect of sensor geometry.

The influence of sensor surface diameter D on peak amplitudes and peak frequency of simulated AE signals is shown in Fig. B1, where the values of peak amplitudes and peak frequency are both normalized by dividing the maximum values. It can be observed that the peak amplitudes and peak frequency both decrease with increasing of sensor diameters.

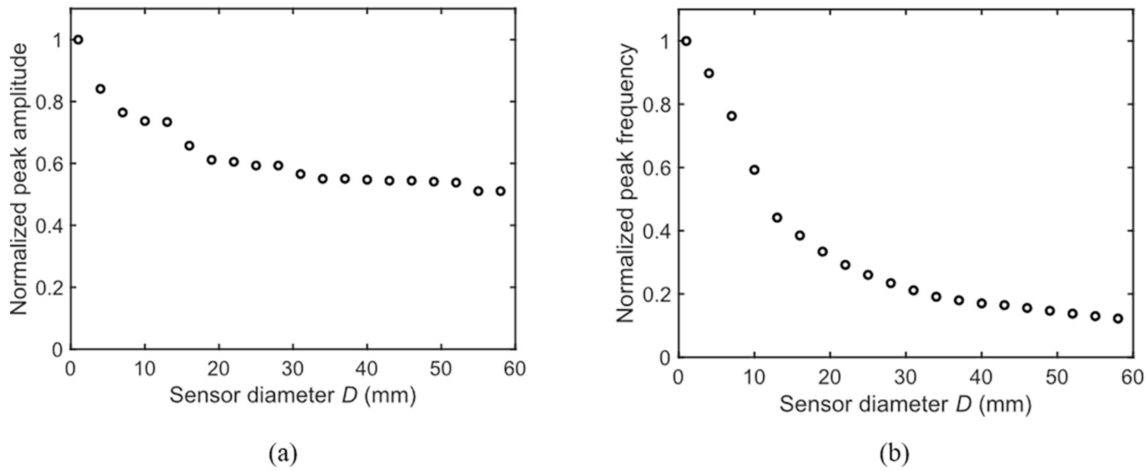

Fig. B1. Influence of sensor surface diameter D on typical parameters of simulated AE parameters: (a) peak amplitudes and (b) peak frequency.

A physical interpretation for above relationships is given in Fig. B2. The sensor surface interferes with the waveform shape in both time and frequency domains, because the output of AE sensor comes from the average disturbance over the entire sensor surface, which is called "aperture" effect [99]. In the time domain, the high-amplitude components are suppressed because of being averaged over sensor surface (Fig. B2a). In the frequency domain, for the frequency components with wavelengths λ less than sensor diameter D, many cycles of the waves (multiple wavelengths) are simultaneously acting on the sensor surface and their contribution is averaged. Such high-frequency components are then filtered by the sensors, as their wavelengths are stretched (Fig. B2b).

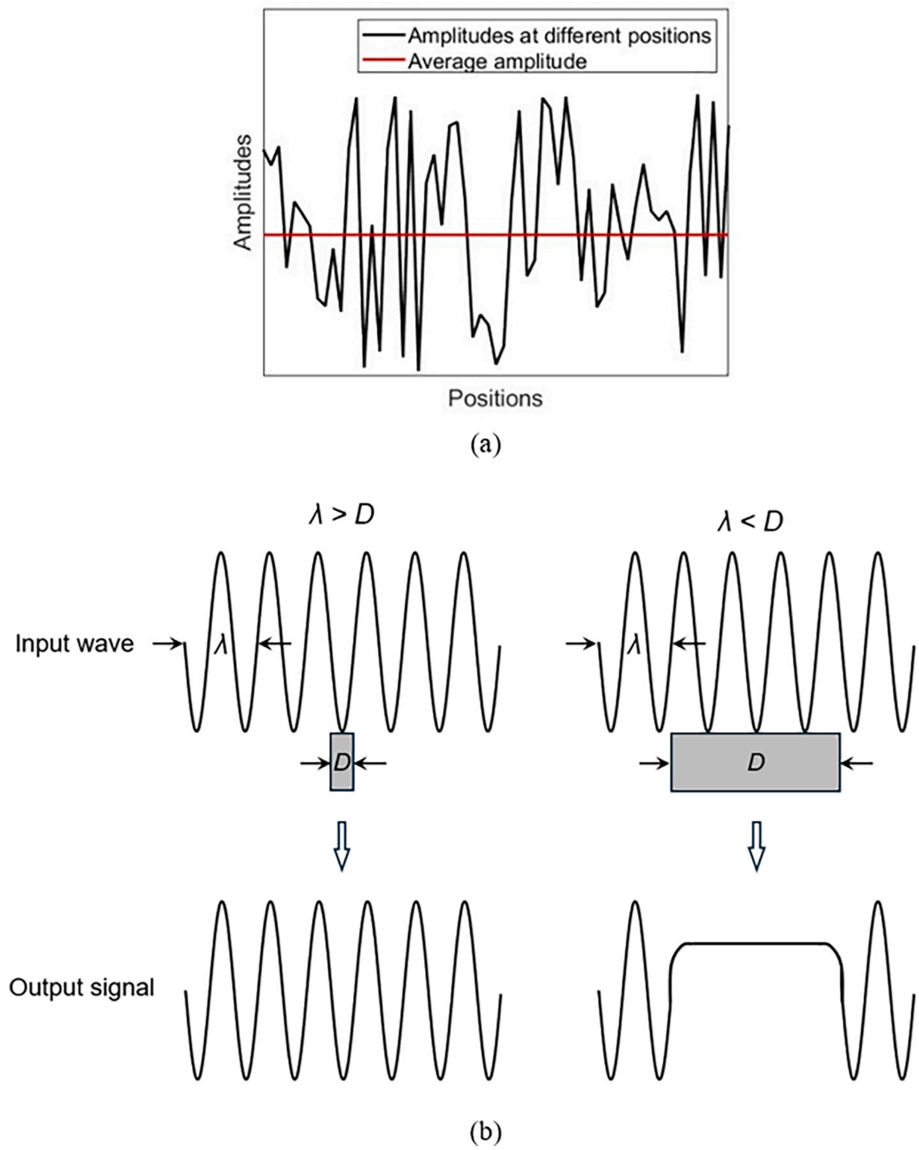

Fig. B2. Physical interpretation for the effect of sensor geometry: (a) time domain and (b) frequency domain.

Data availability

Data will be made available on request.

References

[1] Cuadra JA. A Computational Modeling Approach of Fracture-Induced Acoustic Emission. 2015; Drexel University.
[2] Zhang FQ, et al. *Probability density field of acoustic emission events: Damage identification in concrete structures*. Constr Build Mater 2022;327:126984.
[3] Carpinteri A, et al. *Reliable onset time determination and source location of acoustic emissions in concrete structures*. Cem Concr Compos 2012;34(4):529–37.
[4] Zhang F, et al. *Developing a new acoustic emission source classification criterion for concrete structures based on signal parameters*. Constr Build Mater 2022;318:126163.
[5] Ohno K, Ohtsu M. *Crack classification in concrete based on acoustic emission*. Constr Build Mater 2010;24(12):2339–46.
[6] Chen Z, et al. *Acoustic emission analysis of crack type identification of corroded concrete columns under eccentric loading: A comparative analysis of RA-AF method and Gaussian mixture model*. Case Stud Constr Mater 2023;18:e02021.
[7] Proverbio E. *Evaluation of deterioration in reinforced concrete structures by AE technique*. Mater Corros 2011;62(2):161–9.
[8] Zheng Y, et al. *Localized corrosion induced damage monitoring of large-scale RC piles using acoustic emission technique in the marine environment*. Constr Build Mater 2020;243:118270.

[9] Zheng Y, et al. *Fractal characteristics and damage evaluation of corroded beams under four-point bending tests based on acoustic emission techniques*. Measurement 2022;202:111792.
[10] Dong L, et al. *Uncertainty investigation for the classification of rock micro-fracture types using acoustic emission parameters*. Int J Rock Mech Min Sci 2023;162:105292.
[11] Ohtsu M, Isoda T, Tomoda Y. *Acoustic emission techniques standardized for concrete structures*. Journal of Acoustic Emission 2007;2007(25):21–32.
[12] Iturrioz I, Lacidogna G, Carpinteri A. *Experimental analysis and truss-like discrete element model simulation of concrete specimens under uniaxial compression*. Engng Fract Mech 2013;110:81–98.
[13] Iturrioz I, Lacidogna G, Carpinteri A. *Acoustic emission detection in concrete specimens: Experimental analysis and lattice model simulations*. Int J Damage Mech 2014;23(3):327–58.
[14] Minozzi M, et al. *Dynamic fracture model for acoustic emission*. The European Physical Journal B-Condensed Matter and Complex Systems 2003;36:203–7.
[15] Zhou Y, Aydin BB, Yang Y. Simulation of elastic wave propagation with lattice model. Special Issue of e-Journal of Nondestruct Test (eJNDT) 2024;29(10).
[16] Zhou Y, et al. *A lattice modelling framework for fracture-induced acoustic emission wave propagation in concrete*. Engng Fract Mech 2024;312:110589.
[17] Enoki M, Kishi T. *Theory and analysis of deformation moment tensor due to microcracking*. Int J Fract 1988;38:295–310.
[18] Dahm T. *Relative moment tensor inversion based on ray theory: theory and synthetic tests*. Geophys J Int 1996;124(1):245–57.
[19] Ohtsu M. *Acoustic emission theory for moment tensor analysis*. Res Nondestr Eval 1995;6(3):169–84.
[20] Chang S-H, Lee C-I. *Estimation of cracking and damage mechanisms in rock under triaxial compression by moment tensor analysis of acoustic emission*. Int J Rock Mech Min Sci 2004;41(7):1069–86.
[21] Hazzard JF, Young RP. *Moment tensors and micromechanical models*. Tectonophysics 2002;356(1–3):181–97.
[22] Ohtsu M. *Simplified moment tensor analysis and unified decomposition of acoustic emission source: application to in situ hydrofracturing test*. J Geophys Res Solid Earth 1991;96(B4):6211–21.
[23] Shigeishi M, Ohtsu M. *Acoustic emission moment tensor analysis: development for crack identification in concrete materials*. Constr Build Mater 2001;15(5–6):311–9.
[24] Ohtsu M, Ono K. *The generalized theory and source representations of acoustic emission*. J Acoust Emission 1986;5(4):124–33.
[25] Ohtsu M. *Source kinematics of acoustic emission based on a moment tensor*. NDT Int 1989;22(1):14–20.
[26] Wéber Z. *Estimating source time function and moment tensor from moment tensor rate functions by constrained L 1 norm minimization*. Geophys J Int 2009;178(2):889–900.
[27] Shahidan S, Nor NM, Bunnori NM. *Overview of moment tensor analysis of acoustic emission signal in evaluation concrete structure*. IEEE; 2011.
[28] Ohtsu M. *Acoustic-Emission Theory for Moment Tensor Analysis*. Res Nondestr Eval 1995;6(3):169–84.
[29] Cheng L, et al. *Acoustic emission source location using Lamb wave propagation simulation and artificial neural network for I-shaped steel girder*. Constr Build Mater 2021;273:121706.
[30] Tsangouri E, Aggelis DG. *The influence of sensor size on acoustic emission waveforms—A numerical study*. Appl Sci 2018;8(2):168.
[31] Banerjee S, Mal A. *Acoustic emission waveform simulation in multilayered composites*. J Strain Anal Eng Design 2005;40(1):25–32.
[32] Zelenyak A-M, Hamstad MA, Sause MG. *Modeling of acoustic emission signal propagation in waveguides*. Sensors 2015;15(5):11805–22.
[33] Sause MG, Richler S. *Finite element modelling of cracks as acoustic emission sources*. J Nondestr Eval 2015;34:1–13.
[34] Sause MG, Horn S. *Simulation of acoustic emission in planar carbon fiber reinforced plastic specimens*. J Nondestr Eval 2010;29:123–42.
[35] Prosser WH, et al. *Finite element and plate theory modeling of acoustic emission waveforms*. J Nondestr Eval 1999;18(3):83–90.
[36] Sause MGR, Richler S. *Finite Element Modelling of Cracks as Acoustic Emission Sources*. J Nondestr Eval 2015;34(1):1–13.
[37] Dhatt G, Lefrançois E, Touzot G. Finite element method. 2012; John Wiley & Sons.
[38] Javili A, et al. *Peridynamics review*. Math Mech Solids 2019;24(11):3714–39.
[39] Torii AJ, Machado RD, Arndt M. *GFEM for modal analysis of 2D wave equation*. Engng Comput 2015;32(6):1779–801.
[40] Hamstad MA. *Acoustic emission signals generated by monopole (pencil lead break) versus dipole sources: finite element modeling and experiments*. J Acoust Emiss 2007;25:92–106.
[41] Sause MG, Horn SR. *Influence of specimen geometry on acoustic emission signals in fiber reinforced composites. FEM-Simul Experiment* 2010.
[42] Lisjak A, et al. *Numerical simulation of acoustic emission in brittle rocks by two-dimensional finite-discrete element analysis*. Geophys J Int 2013;195(1):423–43.
[43] Tavarez FA, Plesha ME. *Discrete element method for modelling solid and particulate materials*. Int J Numer Meth Engng 2007;70(4):379–404.
[44] Bićanić N. *Discrete element methods*. Encycl Comput Mech 2004.
[45] Matuttis H-G, Chen J. Understanding the discrete element method: simulation of non-spherical particles for granular and multi-body systems. 2014; John Wiley & Sons.
[46] Wu Y, et al. *Numerical simulation on fracture and acoustic emission behavior of sandstone with partial filling flaw in semi-circular three-point bending tests*. Theor Appl Fract Mech 2023;125:103841.
[47] Wang Z, et al. *Crack propagation process and acoustic emission characteristics of rock-like specimens with double parallel flaws under uniaxial compression*. Theor Appl Fract Mech 2021;114:102983.
[48] Xie C, et al. *Study on failure mechanism of porous concrete based on acoustic emission and discrete element method*. Constr Build Mater 2020;235:117409.
[49] Ji S, Di S. *Discrete element modeling of acoustic emission in rock fracture*. Theor Appl Mech Lett 2013;3(2):021009.
[50] Li S, Smith A. *Relationship between acoustic emission and energy dissipation: a DEM study of soil–structure interaction*. Acta Geotech 2022:1–20.
[51] Gu XQ, et al. *Discrete element modeling of shear wave propagation using bender elements in confined granular materials of different grain sizes*. Comput Geotech 2020;125:103672.
[52] Huang S, et al. *Research on acoustic wave attenuation from the perspective of soil particle movement using the discrete element method*. Comput Electron Agric 2023;207:107747.
[53] Horabik J, Molenda M. *Parameters and contact models for DEM simulations of agricultural granular materials: A review*. Biosyst Engng 2016;147:206–25.
[54] Sadd MH, Adhikari G, Cardoso F. *DEM simulation of wave propagation in granular materials*. Powder Technol 2000;109(1–3):222–33.
[55] Li Z, et al. *Experimental characterization and 3D DEM simulation of bond breakages in artificially cemented sands with different bond strengths when subjected to triaxial shearing*. Acta Geotech 2017;12:987–1002.
[56] Hazzard J, Young R. *Simulating acoustic emissions in bonded-particle models of rock*. Int J Rock Mech Min Sci 2000;37(5):867–72.
[57] Zhang Q, Zhang X-P. *A numerical study on cracking processes in limestone by the b-value analysis of acoustic emissions*. Comput Geotech 2017;92:1–10.
[58] Birck G, et al. *Damage process in heterogeneous materials analyzed by a lattice model simulation*. Engng Fail Anal 2016;70:157–76.
[59] Pan Z, et al. *A review of lattice type model in fracture mechanics: theory, applications, and perspectives*. Engng Fract Mech 2018;190:382–409.
[60] Ostoja-Starzewski M. *Lattice models in micromechanics*. Appl Mech Rev 2002;55(1):35–60.
[61] Kosteski L, et al. *The truss-like discrete element method in fracture and damage mechanics*. Engng Comput 2011;28(6):765–87.
[62] Suiker A, Metrikine A, De Borst R. *Comparison of wave propagation characteristics of the Cosserat continuum model and corresponding discrete lattice models*. Int J Solids Struct 2001;38(9):1563–83.
[63] Zhao G-F. *Developing a four-dimensional lattice spring model for mechanical responses of solids*. Comput Methods Appl Mech Engng 2017;315:881–95.
[64] Zhao GF, Fang J, Zhao J. *A 3D distinct lattice spring model for elasticity and dynamic failure*. Int J Numer Anal Meth Geomech 2011;35(8):859–85.
[65] Chang Z, et al. *Lattice fracture model for concrete fracture revisited: Calibration and validation*. Appl Sci 2020;10(14):4822.
[66] Chang Z, et al. *A discrete lattice model for assessment of buildability performance of 3D-printed concrete*. Comput-Aided Civil Infrastruct Eng 2021;36(5):638–55.
[67] Li W-J, Zhu Q-Z. *An innovative quasi-bond approach to bridge continuity, anisotropic damage and macroscopic fracture of solids and structures*. Int J Plast 2024;172:103829.
[68] Nikolić M, et al. *Lattice element models and their peculiarities*. Arch Comput Meth Engng 2018;25:753–84.
[69] Grabec I, Petrišič J. *The application of a semielastic lattice model to the description of acoustic emission*. Engng Fract Mech 1986;23(4):621–9.
[70] Trochidis A, Polyzos B. *Acoustic emission during plastic deformation of crystals: A lattice-dynamics approach*. J Appl Phys 1995;78(1):170–5.

[71] Nagy E, Landis EN, Davids WG. Acoustic emission measurements and lattice simulations of microfracture events in spruce; 2010.
[72] Grégoire D, et al. *Mesoscale analysis of failure in quasi-brittle materials: comparison between lattice model and acoustic emission data*. Int J Numer Anal Meth Geomech 2015;39(15):1639–64.
[73] Sagar RV, et al. *Modeling mode-I fracture process in concrete at meso-scale: Computational aspects of lattice model and a comparison between results of two dimensional lattice simulation and acoustic emission measurements*. Engng Fract Mech 2019;210:257–78.
[74] Sagar RV, Prasad BR. *Fracture analysis of concrete using singular fractal functions with lattice beam network and confirmation with acoustic emission study*. Theor Appl Fract Mech 2011;55(3):192–205.
[75] Friedrich LF, et al. *Analysis of acoustic emission activity during progressive failure in heterogeneous materials: experimental and numerical investigation*. Appl Sci 2022;12(8):3918.
[76] Rodrigues RS, Birck G, Iturrioz I. *Damage index proposals applied to quasi-brittle materials simulated using the lattice discrete element method*. Int J Damage Mech 2016;25(7):1017–39.
[77] Aydin BB, Tuncay K, Binici B. *Overlapping lattice modeling for concrete fracture simulations using sequentially linear analysis*. Struct Concr 2018;19(2):568–81.
[78] Aydin BB, et al. *Lattice modeling and testing of aerated autoclaved concrete infilled frames*. Engng Struct 2022;251:113467.
[79] Aydin BB, Binici B, Tuncay K. *Lattice simulation of concrete compressive behaviour as indirect tension failure*. Mag Concr Res 2021;73(8):394–409.
[80] Aydin BB, Tuncay K, Binici B. *Simulation of reinforced concrete member response using lattice model*. J Struct Engng 2019;145(9):04019091.
[81] Hrennikoff A. Solution of problems of elasticity by the framework method; 1941.
[82] Rinaldi A, et al. *Lattice models of polycrystalline microstructures: A quantitative approach*. Mech Mater 2008;40(1–2):17–36.
[83] Bažant ZP, Oh BH. *Crack band theory for fracture of concrete*. Matériaux et construction 1983;16:155–77.
[84] Cornelissen H, Hordijk D, Reinhardt H. *Experimental determination of crack softening characteristics of normalweight and lightweight*. Heron 1986;31(2):45–6.
[85] Chung J, Lee JM. *A new family of explicit time integration methods for linear and non-linear structural dynamics*. Int J Numer Meth Engng 1994;37(23):3961–76.
[86] Liu M, Gorman DG. *Formulation of Rayleigh Damping and Its Extensions*. Comput Struct 1995;57(2):277–85.
[87] Johnson MA, Moradi MH. PID control. 2005: Springer.
[88] Ziegler JG, Nichols NB. *Optimum settings for automatic controllers*. Trans Am Soc Mech Engng 1942;64(8):759–65.
[89] Walraven JC. Model Code 2010-Final Draft: Volume 1. Vol. 65. 2012: fib Fédération internationale du béton.
[90] MISTRAS. R15α Sensor. 2011: Princeton Jctction, NJ 08550, USA, Products & System Division.
[91] PAC. DiSP with AEwin User's Manual Rev. 3. 2005, Physical Acoustic Corporation: Princeton, New Jersey, USA.
[92] Haldorsen JB. Spatial aliasing. In: SEG International Exposition and Annual Meeting. 2020. OnePetro.
[93] Carpinteri A, Accornero F. *Multiple snap-back instabilities in progressive microcracking coalescence*. Engng Fract Mech 2018;187:272–81.
[94] Madariaga R. *High-Frequency Radiation from Crack (Stress Drop) Models of Earthquake Faulting*. Geophys J R Astron Soc 1977;51(3):625–51.
[95] Carpinteri A, et al. *Cracking and crackling in concrete-like materials: A dynamic energy balance*. Engng Fract Mech 2016;155:130–44.
[96] Schlangen E, Garboczi EJ. *Fracture simulations of concrete using lattice models: computational aspects*. Engng Fract Mech 1997;57(2–3):319–32.
[97] Caleap M, Aristégui C, Angel YC. *Effect of crack opening and orientation on dispersion and attenuation of antiplane coherent wave*. Geophys J Int 2009;177(3):1151–65.
[98] Unnþórsson R. *Hit detection and determination in AE bursts*. Acoustic emission-research and applications 2013:1–20.
[99] Grosse CU, et al. Acoustic emission testing: Basics for research–applications in engineering. 2021: Springer Nature.